



CERN-PH-TH-2015-202

CP3-15-27

TIF-UNIMI-2015-5

PREPARED FOR SUBMISSION TO JHEP

On the Impact of Lepton PDFs

Valerio Bertone,^a Stefano Carrazza,^b Davide Pagani,^c Marco Zaro.^{d,e}

^a*PH Department, TH Unit,
CERN, CH-1211 Geneva 23, Switzerland*

^b*Dipartimento di Fisica, Università di Milano and INFN, Sezione di Milano,
Via Celoria 16, I-20133 Milano, Italy*

^c*Center for Cosmology, Particle Physics and Phenomenology (CP3)
Université Catholique de Louvain, B-1348 Louvain-la-Neuve, Belgium*

^d*Sorbonne Universités, UPMC Univ. Paris 06, UMR 7589, LPTHE, F-75005, Paris, France*

^e*CNRS, UMR 7589, LPTHE, F-75005, Paris, France*

E-mail: valerio.bertone@cern.ch, stefano.carrazza@mi.infn.it,
davide.pagani@uclouvain.be, marco.zaro@lpthe.jussieu.fr

ABSTRACT: In this paper we discuss the effect of the complete leading-order QED corrections to the DGLAP equations that govern the perturbative evolution of parton distribution functions (PDFs). This requires the extension of the purely QCD DGLAP evolution including a PDF for the photons and, consistently, also for the charged leptons e^\pm , μ^\pm and τ^\pm . We present the implementation of the QED-corrected DGLAP evolution in the presence of photon and lepton PDFs in the APFEL program and, by means of different assumptions for the initial scale PDFs, we produce for the first time PDF sets containing charged lepton distributions. We also present phenomenological studies that aim to assess the impact of the presence of lepton PDFs in the proton for some relevant SM (and BSM) processes at the LHC at 13 TeV and the FCC-hh at 100 TeV. The impact of the photon PDF is also outlined for those processes.

KEYWORDS: parton distribution functions, electroweak corrections, high-precision computation

Contents

1	Introduction	1
2	PDFs determination	3
2.1	DGLAP equations in the presence of photons and leptons	3
2.2	Modelling the lepton PDFs	5
2.3	PDF sets with lepton distributions	6
3	Phenomenological impact	11
3.1	Parton luminosities	11
3.2	Production processes	15
4	Conclusions and outlook	27
A	The combined QCD+QED evolution in the presence of lepton PDFs	29

1 Introduction

The Run II at the Large Hadron Collider (LHC) will probe the interactions of elementary particles at unprecedented scales of energy and with an outstanding accuracy. In order to correctly identify possible Beyond-the-Standard-Model (BSM) effects, the theoretical predictions for the Standard Model (SM) processes have to match (at least) the precision of the corresponding experimental measurements. In other words, the impact of higher-order corrections on phenomenological predictions has to be known and under control. To this purpose, the computation of Next-to-Leading-Order (NLO) QCD corrections is necessary, but often not sufficient. For example, at fixed order the inclusion of the second-order (NNLO) corrections in QCD as well as of the NLO electroweak (EW) corrections is in general desirable and in particular cases even essential. In order to formally achieve this level of accuracy, not only the matrix elements of the hard processes, but also the so-called parton-distribution functions (PDFs) have to be known at the same level of precision. While most of the collaborations already provide PDF sets accurate up to NNLO in QCD [1–5], for the EW corrections the situation is less satisfactory. Indeed, NLO EW corrections naturally introduce photon-induced processes and only two PDF sets including a photon density are presently available: the MRST2004QED set [6], whose photon PDF is determined by means of model assumptions, and the NNPDF2.3QED family [7], where instead the photon PDF is extracted by means of a fit to data. Contrary to the MRST2004QED set, the photon PDF of NNPDF2.3QED sets is provided with an uncertainty. In addition, the aforementioned PDF sets are accurate up to (N)NLO in QCD but only at LO in QED evolution. Thus, since NLO EW, and in particular NLO QED effects,

are never included at the level of PDFs, this level of accuracy cannot be formally claimed at the level of the hadronic cross section.

Before moving to NLO QED accuracy, however, it is worth attempting a determination of PDFs at (N)NLO QCD + LO QED accuracy for all the QED-interacting SM particles, *i.e.* by considering also *leptons* as partons of the proton. In this way predictions for lepton-induced processes at hadron colliders could be easily calculated by convoluting partonic cross sections with lepton PDFs. On the one hand, this can be useful for the study of processes such as same-sign and/or different-flavour dilepton production, which, with lepton PDFs, can be directly produced without requiring additional (unresolved) jets or photons. On the other, lepton-initiated processes are naturally involved in EW corrections. Indeed, as already mentioned, a very interesting aspect of EW corrections is the fact that they naturally require new partons in the proton on top of the usual (anti)quarks and gluons. Processes with quarks in the initial state at LO receive NLO EW corrections from photon-initiated processes. Equivalently, once the photon is considered as a parton, photon-initiated processes at LO will receive corrections from processes including leptons in the initial state. However, while PDF fits that provide an estimate of the photon PDFs are presently available, this is not the case for leptons.

There are (at least) two reasons why lepton PDFs have been neglected so far in the context of EW corrections. Firstly, they are expected to be small, since they are suppressed by a factor α with respect to the photon PDF, which in turn is already suppressed with respect to quark and gluon PDFs. Secondly, photon-initiated processes are typically simulated only at LO accuracy, due the smallness of the photon PDF with respect to quark and gluon ones. Thus, neglecting NLO EW corrections in photon-initiated processes, the absence of the lepton PDFs has never been a real issue. On the other hand, the recent progresses in the automation of NLO EW corrections [8–12] make it possible to take into account these contributions without additional efforts. Moreover, lepton PDFs can induce not only EW corrections, but also new LO contributions for many SM and BSM processes at hadron colliders. In particular, leptons in the initial state can open new production mechanisms. For instance, at LO the production of a lepton pair can proceed also through a *t*-channel photon exchange as it is the case for the elastic scattering at lepton colliders. This production mechanism is enhanced in the peripheral region close to the beam pipe, therefore a quantitative estimate of lepton PDFs is desirable in order not to introduce any systematic effect in the searches and measurements in the Run II at the LHC and possibly also at future colliders.

The purpose of this paper is to give the first quantitative estimate on the leptonic content of the proton and analyse its phenomenological impact at the LHC at 13 TeV and at a future 100 TeV hadron-hadron collider (FCC-hh). This will be achieved in two steps. First of all by implementing the lepton PDF Dokshitzer-Gribov-Altarelli-Lipatov-Parisi (DGLAP) evolution equations at LO in QED in the so-called variable-flavour-number (VFN) scheme in the evolution code **APFEL** [13], and secondly by producing a guess for the lepton PDFs at the initial scale based on the assumption that leptons are generated by photon splitting at the respective mass scales.

The paper is organised as follows. In Section 2 we describe the procedure used to

generate new PDF sets including leptons. First, in Section 2.1 we show how to generalise the DGLAP evolution equations in order to include the complete QED corrections at LO, which involve leptons. Then, in Section 2.2 we discuss how to model the lepton distributions at the initial scale on the base of different theoretical assumptions. In Section 2.3 we present the numerical results obtained with APFEL, considering different initial conditions and comparing the results at the level of PDFs and momentum fractions. In Section 3 we discuss the phenomenological impact of lepton (and photon) PDFs at the LHC and at the FCC-hh. In Section 3.1 we look at the impact of lepton PDFs on parton luminosities and we analyse their dependence on the invariant mass and the rapidity of the initial/final state in a process-independent approach. Then, in Section 3.2, we turn to the study of the effects of lepton PDFs for some relevant SM (and BSM) processes at the LHC and at the FCC-hh. Finally, in Section 4, we draw our conclusions and discuss possible phenomenological studies that could be done using PDF sets with lepton distributions. The PDF grids used in this work have been made public in the LHAPDF6 library [14] format.

2 PDFs determination

2.1 DGLAP equations in the presence of photons and leptons

In this section we will show how to extend the DGLAP equations in order to include the evolution of photon and lepton PDFs at leading order (LO) in QED. The inclusion of the photon PDF evolution has already been treated extensively in Refs. [6, 13, 15] and thus we will not discuss it here. As far as leptons are concerned, at LO in QED they couple directly only to photons. However, since the photons couple to quarks that in turn couple to gluons, the lepton PDFs evolution will indirectly depend on the evolution of all other partons. Following the notation of Ref. [13], where QCD and QED evolutions are treated separately, the inclusion of leptons does not imply any change to the pure QCD sector. On the contrary, with the inclusion of leptons, the QED evolution equations with respect to the QED factorisation scale ν read:

$$\begin{aligned}
\nu^2 \frac{\partial \gamma}{\partial \nu^2} &= \frac{\alpha}{4\pi} \left[\left(\sum_q^{n_f} N_c e_q^2 \right) P_{\gamma\gamma}^{(0)} \otimes \gamma + \sum_q^{n_f} e_q^2 P_{\gamma q}^{(0)} \otimes (q + \bar{q}) + \sum_\ell^{n_\ell} P_{\gamma\ell}^{(0)} \otimes (\ell^- + \ell^+) \right], \\
\nu^2 \frac{\partial q}{\partial \nu^2} &= \frac{\alpha}{4\pi} \left[N_c e_q^2 P_{q\gamma}^{(0)} \otimes \gamma + e_q^2 P_{qq}^{(0)} \otimes q \right], \\
\nu^2 \frac{\partial \bar{q}}{\partial \nu^2} &= \frac{\alpha}{4\pi} \left[N_c e_q^2 P_{q\gamma}^{(0)} \otimes \gamma + e_q^2 P_{q\bar{q}}^{(0)} \otimes \bar{q} \right], \\
\nu^2 \frac{\partial \ell^-}{\partial \nu^2} &= \frac{\alpha}{4\pi} \left[P_{\ell\gamma}^{(0)} \otimes \gamma + P_{\ell\ell}^{(0)} \otimes \ell^- \right], \\
\nu^2 \frac{\partial \ell^+}{\partial \nu^2} &= \frac{\alpha}{4\pi} \left[P_{\ell\gamma}^{(0)} \otimes \gamma + P_{\ell\ell}^{(0)} \otimes \ell^+ \right],
\end{aligned} \tag{2.1}$$

where γ , $q(\bar{q})$ and $\ell^-(\ell^+)$ correspond to the PDFs of the photon, the quark(antiquark) flavour q and the lepton(antilepton) species ℓ , respectively. In Eq. (2.1), e_q corresponds to

the electric charge of the quark flavour q , $N_c = 3$ is the number of QCD colours and α is the running fine-structure constant. Note also that the indices q and ℓ in the sums in the first line of Eq. (2.1) run over the n_f and n_ℓ active quarks and leptons at the scale ν , respectively. The symbol \otimes represents the usual Mellin convolution operator defined as:

$$A(x) \otimes B(x) \equiv \int_0^1 dy \int_0^1 dz A(y) B(z) \delta(x - yz). \quad (2.2)$$

Finally, the LO QED splitting functions $P_{ij}^{(0)}$ are given by:

$$\begin{aligned} P_{\gamma\gamma}^{(0)}(x) &= -\frac{4}{3}\delta(1-x), \\ P_{q\gamma}^{(0)}(x) &= P_{\ell\gamma}^{(0)}(x) = 2[x^2 + (1-x)^2], \\ P_{\gamma q}^{(0)}(x) &= P_{\gamma\ell}^{(0)}(x) = 2\left[\frac{1 + (1-x)^2}{x}\right], \\ P_{qq}^{(0)}(x) &= P_{\ell\ell}^{(0)}(x) = 2\frac{1+x^2}{(1-x)_+} + 3\delta(1-x). \end{aligned} \quad (2.3)$$

Combining the system of differential equations in Eq. (2.1) with the pure-QCD DGLAP equations that govern the evolution of gluons and quarks, we obtain the full (N)NLO QCD plus LO QED evolution in the presence of photons and leptons. The solution of this system is implemented in version 2.4.0, or later, of the **APFEL** evolution library [13].

It is worth stressing that, contrary to the approach described in the original reference of **APFEL** [13], in the new implementation of the coupled QCD+QED DGLAP equations the QCD and the QED evolutions are no longer treated separately and combined *a posteriori*. Indeed, thanks to a suitable combination of PDFs that cleverly diagonalises the full splitting-function matrix in the presence of QED corrections, we have been able to implement in **APFEL** an efficient *unified* solution of the QCD+QED DGLAP equations where the evolution of PDFs with respect to QCD and QED factorisation scales takes place at the same time. In other words, QCD and QED factorisation scales are no longer kept separate and are instead identified. We present the details of this basis in Appendix A.

As far as the fine-structure constant α is concerned, consistently with the evolution of PDFs, we only consider the LO running by solving the renormalisation-group equation:

$$\nu^2 \frac{d\alpha}{d\nu^2} = \beta_{\text{QED}}^{(0)} \alpha^2(\nu), \quad (2.4)$$

with:

$$\beta_{\text{QED}}^{(0)} = \frac{8}{12\pi} \left(N_c \sum_q^{n_f} e_q^2 + n_\ell \right), \quad (2.5)$$

where, as a boundary condition for the evolution, we take $\alpha^{-1}(m_\tau) = 133.4$.

2.2 Modelling the lepton PDFs

Once the full QCD+QED DGLAP evolution in the presence of photons and leptons has been implemented, the following step is the determination of suitable boundary conditions, *i.e.* the initial scale PDFs, to be evolved. As far as gluons and quarks are concerned, various solid determinations are publicly available [1–5]. On the other hand, as already mentioned, only two public determinations of the photon PDF are available at the moment: the MRST2004QED set [6], where the photon PDF is determined by means of a model assumption, and the more recent NNPDF2.3QED family [7], where the photon PDF is instead determined from a fit to data. No lepton PDF determination has ever been attempted so far.

In principle, the most reliable way to determine the lepton PDFs is the extraction from data by means of a fit. However, to our opinion, this option is currently not viable. The main reason is that lepton PDFs are expected to be tiny as compared to the quark and gluon ones and even substantially smaller than the photon PDF. Assuming no intrinsic leptonic component in the proton, lepton PDFs are expected to be of the order of α times the photon PDF, where $\alpha \sim 10^{-2}$. As a consequence, the photon being already suppressed as compared to quark and gluon PDFs, the contribution of leptons is likely to be so small that the determination of the corresponding PDFs from experimental data is hardly achievable.

As an alternative to the fit, one could try to guess the functional form of the lepton PDFs just by assuming that light leptons, *i.e.* electrons and muons, are generated by photon splitting at the respective mass scales. Using the leading-logarithmic (LL) approximation for the photon splitting into leptons, one can then infer their distributions at the initial scale $Q_0 \simeq 1$ GeV as:

$$\ell^-(x, Q_0) = \ell^+(x, Q_0) = \frac{\alpha(Q_0)}{4\pi} \ln \left(\frac{Q_0^2}{m_\ell^2} \right) \int_x^1 \frac{dy}{y} P_{\ell\gamma}^{(0)} \left(\frac{x}{y} \right) \gamma(y, Q_0), \quad (2.6)$$

with $\ell = e, \mu$ ¹. In other words, Eq. (2.6) comes from the linearisation of the LO QED DGLAP evolution for the lepton PDFs ℓ^\pm from the mass scale m_ℓ , where they are assumed to appear as dynamical partons, to the initial scale Q_0 . Indeed, in the situation where both QED and QCD evolutions are considered, the divergence of the strong coupling α_s in correspondence of Λ_{QCD} (Landau pole), with $\Lambda_{\text{QCD}} > m_\ell$, makes such evolution impossible to implement in an exact way and Eq. (2.6) represents an approximated solution. Thus, Eq. (2.6) is equivalent to assume that the photon PDF does not evolve between the lepton mass scale m_ℓ and the initial scale Q_0 . However, the DGLAP evolution between m_ℓ and Q_0 would introduce additional $\mathcal{O}(\alpha)$ terms that exceed the LO QED accuracy.

Since the tau mass is typically larger than Q_0 ($m_\tau = 1.777$ GeV $\gtrsim Q_0$), we have chosen to determine the τ^\pm PDFs according to the usual VFN scheme [17–19], *i.e.* by dynamically generating them at the threshold.

ID	PDF Set	Ref.	QCD	QED	Photon PDF	Lepton PDFs
A1	apfel_nn23nlo0118_lept0	[20]	NLO	LO	$\gamma(x, Q_0) = 0$	Eq. (2.7)
A2	apfel_nn23nnlo0118_lept0	[20]	NNLO	LO	$\gamma(x, Q_0) = 0$	Eq. (2.7)
B1	apfel_nn23qedlo0118_lept0	[21]	LO	LO	Internal	Eq. (2.7)
B2	apfel_nn23qednlo0118_lept0	[7]	NLO	LO	Internal	Eq. (2.7)
B3	apfel_nn23qednnlo0118_lept0	[7]	NNLO	LO	Internal	Eq. (2.7)
B4	apfel_mrsto4qed_lept0	[6]	NLO	LO	Internal	Eq. (2.7)
C1	apfel_nn23qedlo0118_lept	[21]	LO	LO	Internal	Eq. (2.6)
C2	apfel_nn23qednlo0118_lept	[7]	NLO	LO	Internal	Eq. (2.6)
C3	apfel_nn23qednnlo0118_lept	[7]	NNLO	LO	Internal	Eq. (2.6)
C4	apfel_mrsto4qed_lept	[6]	NLO	LO	Internal	Eq. (2.6)

Table 1: Summary of the sets of PDFs including photons and leptons generated with APFEL.

2.3 PDF sets with lepton distributions

In this section we discuss the results of the implementation of the lepton PDF evolution in APFEL. As discussed in the previous section, the determination of lepton PDFs from a direct fit to data seems to be hard to achieve and thus, as an alternative, we adopt a model based on a theoretical assumption for modelling lepton PDFs at the initial scale.

The model presented in the previous section is based on the assumption that leptons are generated in pairs from LL photon splitting at the respective mass scales. This results in the ansatz in Eq. (2.6) for the light lepton PDFs. However, in order to test how sensitive the results are with respect to the initial scale distributions, we also consider the “zero-lepton” ansatz where the lepton PDFs at the initial scale Q_0 are (artificially) set to zero, that is:

$$\ell^-(x, Q_0) = \ell^+(x, Q_0) = 0. \quad (2.7)$$

In this context, the construction of PDF sets with leptons requires a pre-existing PDF set to which we add our models for the lepton distributions. Of course, in order to apply the ansatz in Eq. (2.6), we need PDF sets that already contain a photon PDF, *e.g.* the MRST2004QED set [6] or the NNPDF2.3QED sets [7]. We will use both sets to generate lepton PDFs via the ansatz in Eq. (2.6). On the contrary, the ansatz in Eq. (2.7) can be applied to any set so that lepton and photon distributions are generated just by DGLAP evolution.

In order to assess the effect of considering lepton PDFs in the DGLAP evolution, we consider three different initial-scale configurations that are also summarised in Tab. 1:

- sets where both photon and lepton PDFs are initially absent and dynamically generated by DGLAP evolution. For this configuration we have constructed the sets A1 and A2 in Table 1 based on NNPDF2.3 NLO and NNLO, respectively.
- Sets where the photon distribution is present and the lepton PDFs are set to zero at the initial scale Q_0 (*i.e.* Eq. (2.7)) and then evolved as discussed in Sect. 2.1. These

¹For the light lepton masses, we take $m_e = 0.510998928$ MeV and $m_\mu = 105.6583715$ MeV, as quoted in the PDG [16].

configurations are based on the NNPDF2.3QED and MRST2004QED sets of PDFs and identified by the indices B1, B2, B3 and B4 in Table 1.

- Sets of PDFs generated from NNPDF2.3QED and MRST2004QED using the ansatz in Eq. (2.6) for the light lepton PDFs (sets C1, C2, C3 and C4 in Table 1).

The evolution of the PDF sets listed in Tab. 1 is performed using APFEL, as discussed in Sect. 2.1. All PDF sets are tabulated in the LHAPDF6 format, which allows us to include the lepton PDFs in a straightforward manner. In the following we will present the results of the implementation of the lepton PDF evolution for the different ansätze discussed above. In particular, we will quantify momentum fractions, correlations and the differences among the different sets. In order to make the discussion more concise, we will only presents results for the NLO sets. However, the features we observe are common to all sets and thus all the conclusions we draw apply also to LO and NNLO sets.

In Fig. 1 we show the lepton and photon PDF central values for the set identified by the ID A1 in Table 1. In this configuration photons and leptons are set to zero at $Q_0 = 1$ GeV and then dynamically generated by DGLAP evolution. The left plot shows PDFs at $Q = 1.8$ GeV, in this case electron and muon PDFs are identical (by definition), and the τ PDF has just been dynamically generated ($m_\tau = 1.777$ GeV). In the right plot the same comparison is displayed at $Q = 100$ GeV, showing that all lepton PDFs are close to each other. Similar results are obtained also with the NNPDF2.3 NNLO (A2) set.

Configurations B2 and B4 are shown in Fig. 2. In this case, the prior sets of PDFs contain a photon PDF while lepton PDFs are null at the initial scale Q_0 and thus generated dynamically by DGLAP evolution. Again, similar results are obtained for the NNPDF2.3QED LO (B1) and NNLO (B3) sets.

Finally, we consider the configurations of type C where, starting from a prior containing a photon PDF, the initial distributions for the leptons are determined using the ansatz in Eq. (2.6). In Fig. 3 we show the resulting lepton PDFs for the configurations C2 (top) and C4 (bottom), at $Q = 1.8$ GeV (left) and $Q = 100$ GeV (right). Again, the qualitative behaviour for the configurations C1 and C3 is the same.

Fig. 4 shows the ratios for the light lepton PDFs at $Q = 100$ GeV for the configurations A1, B2, C2 to C4. In this way we can quantify the difference generated by the various initial conditions starting from the same prior set, *i.e.* NNPDF2.3 at NLO. For the electron PDFs (left plot), the ansätze in Eqs. (2.6) and (2.7) applied to a set with a photon PDF leads to similar results in the small- x region, while differences up to 50% are observed in the large- x region. The electron PDFs resulting from the set without a photon PDF are instead much smaller for all in the entire x range. The same behaviour is observed also for the muon PDFs (right plot in Fig. 4), with slightly less enhanced discrepancies as compared to electrons.

As already mentioned, the photon PDF of the NNPDF2.3QED sets is provided with an uncertainty. This enables us to assess how compatible the lepton PDFs emerging from the three different configurations described above are. In Fig. 5 we show the same plots presented in Fig. 4 but including the 68% confidence level (CL) bands (when available). We

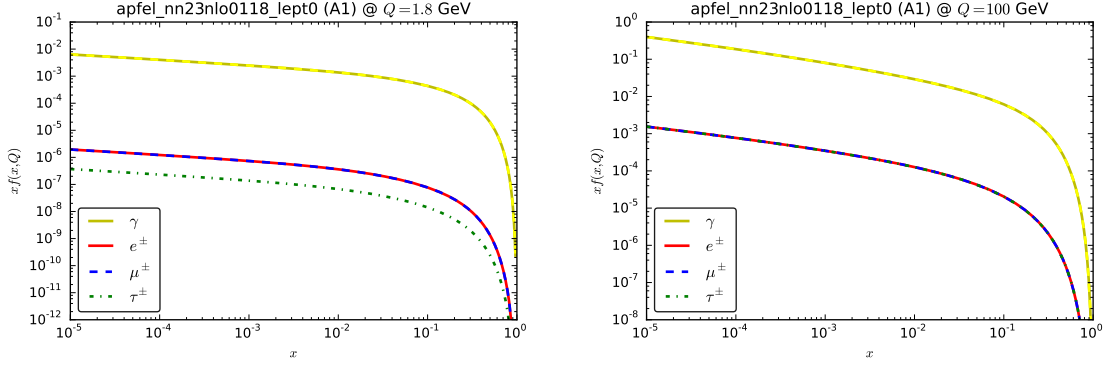


Figure 1: Lepton and photon PDFs for the configuration A1 at $Q = 1.8$ GeV (left) and $Q = 100$ GeV (right).

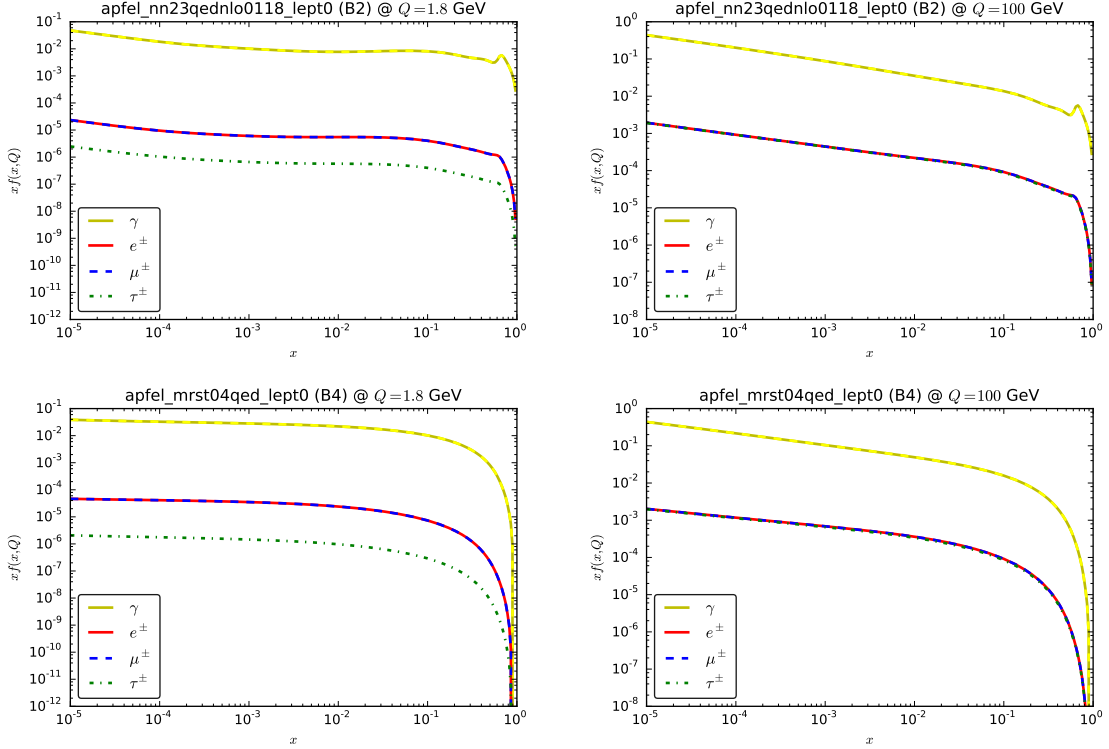


Figure 2: Same as Fig. 1 for the configurations B2 (top) and B4 (bottom).

observe that the configurations B2 and C2 are perfectly compatible within uncertainties all over the range in x . We can thus conclude that, even though the ansatz in Eq. (2.6) provides an arguably better estimate of the lepton PDFs, the present precision with which the photon PDF is determined is such that the difference with respect to the “zero-lepton” ansatz in Eq. (2.7) is still within uncertainties. Finally, it is unsurprising that the configuration A1, that has no uncertainty band because it assumes that the photon PDF is identically zero at the initial scale for all PDF replicas, lies right on the lower limit of the

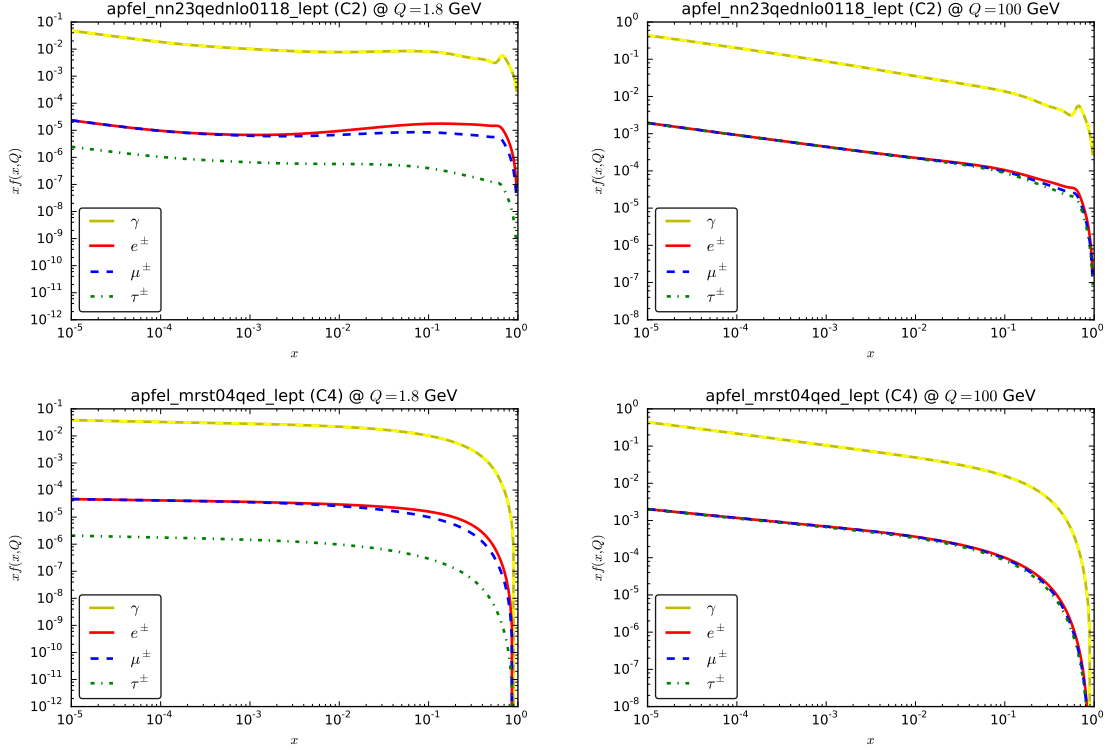


Figure 3: Same as Fig. 1 for the configurations C2 (top) and C4 (bottom).

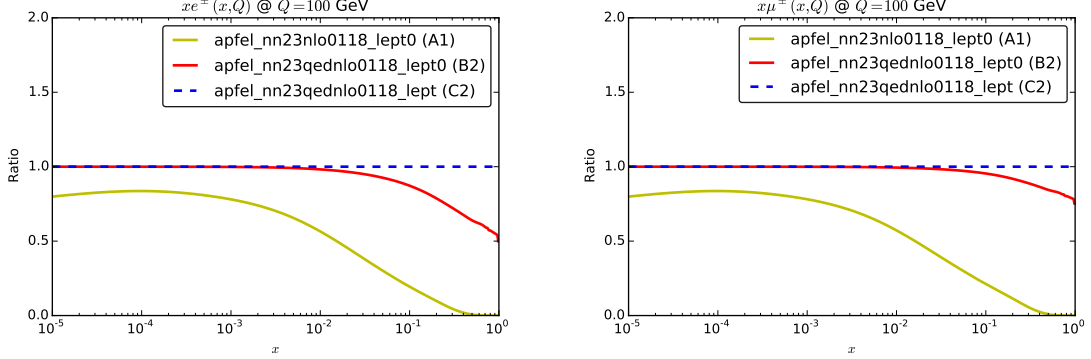


Figure 4: Electron (left) and muon (right) PDFs at $Q = 100$ GeV for the configurations A1, B2 and C2, displayed as ratios to C2.

uncertainty band of both configurations B2 and C2. The reason for this can be traced back to the fact the the photon PDF of the NNPDF2.3QED sets at the initial scale is compatible with zero and, due to the enforcement of positivity, the lower limit of the 68% CL band essentially coincides with $\gamma(x, Q_0) = 0$.

Interesting information about the photon and lepton content of the proton is provided

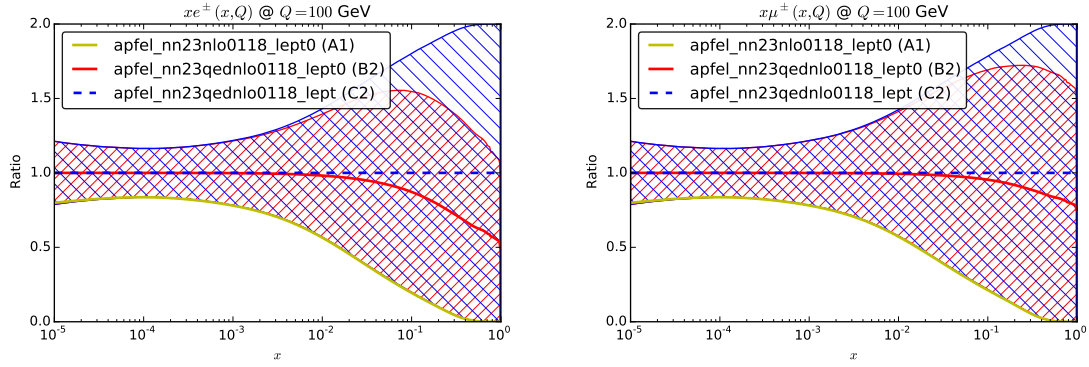


Figure 5: Same as Fig. 4 but with 68% CL bands displayed.

by the respective momentum fractions defined as:

$$\text{MF}_\gamma(Q) = \int_0^1 dx x \gamma(x, Q), \quad \text{and} \quad \text{MF}_{\ell^\pm}(Q) = \int_0^1 dx x \ell^\pm(x, Q). \quad (2.8)$$

In Fig. 6 we plot the percent momentum fractions as a function of the scale Q for the configurations B2 (left) and C2 (right). While the photon PDF carries up to around 1% of the momentum fraction of the proton, lepton PDFs carry a much smaller fraction (by about two orders of magnitude), regardless of the initial-scale parameterisation. This is consistent with the fact that, for both parameterisations, lepton PDFs are proportional to α times the photon PDF ($\ell \propto \alpha \times \gamma$). In conclusion, lepton PDFs carry such a small fraction of the proton momentum that they do not cause a significant violation of the total momentum sum rule when attached to a pre-existing PDF set.

Now we turn to consider the uncertainties of the lepton PDFs. A realistic estimate of the lepton PDFs also requires an estimate of the respective uncertainties. To this end, using exactly the same procedure discussed in the previous sections, we have generated lepton PDFs for all replicas of the NNPDF2.3 family sets. This allows one to estimate the uncertainty on each lepton PDF in the usual way. In Fig. 7 we plot the lepton PDFs with the respective uncertainty for the configurations C2 and C3 at $Q = 100$ GeV. Uncertainties are presented as symmetric 68% CL bands centred around the mean value of each PDF. As expected, the lepton PDF uncertainties follow the pattern of the photon PDF, characterised by a large uncertainty at large x .

To conclude this section, in Fig. 8 we present the PDF correlation matrix for the configuration C3 at $Q = 1.8$ GeV on a grid of $N_x = 50$ points logarithmically distributed in the interval $x_1, x_2 = [10^{-5}, 0.9]$, for the partons $\tau, \mu, e, \gamma, g, d, u$ and s . The correlation coefficients are defined as:

$$\rho_{\alpha\beta}(x_1, x_2, Q) = \frac{N_{\text{rep}}}{N_{\text{rep}} - 1} \left(\frac{\langle f_\alpha(x_1, Q) f_\beta(x_2, Q) \rangle_{\text{rep}} - \langle f_\alpha(x_1, Q) \rangle_{\text{rep}} \langle f_\beta(x_2, Q) \rangle_{\text{rep}}}{\sigma_\alpha(x_1, Q) \cdot \sigma_\beta(x_2, Q)} \right), \quad (2.9)$$

where averages are taken over the N_{rep} replicas and where $\sigma_i(x, Q)$ are the corresponding standard deviations.

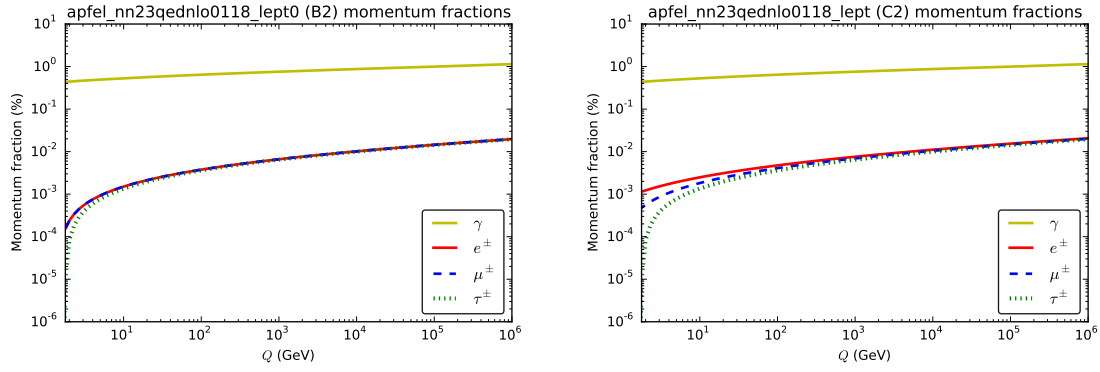


Figure 6: Momentum fractions for the photon and lepton PDFs.

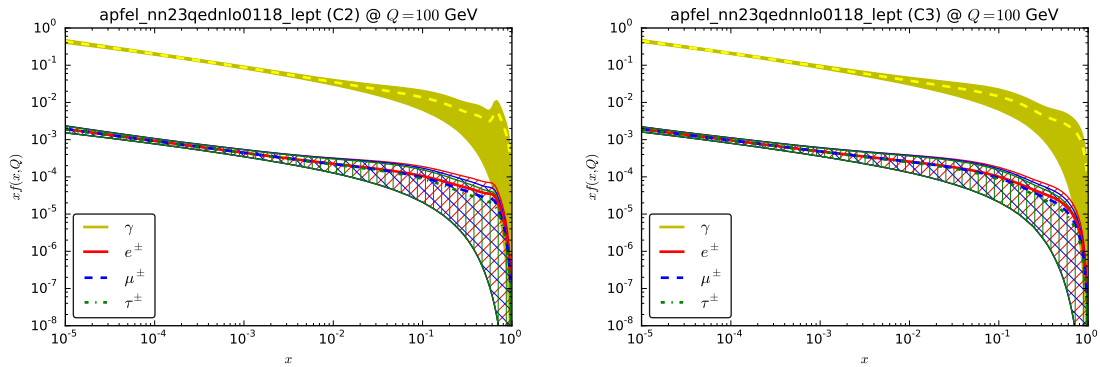


Figure 7: Uncertainty bands for the photon and the lepton PDFs of configurations C2 (left) and C3 (right) at $Q = 100$ GeV.

We note a clear distinction between the QED (top-left square region) and the QCD sector (bottom-right region). As expected, there are strong correlations between τ , μ , e and γ due to the fact that leptons are generated by photon splitting. A similar but milder behaviour is also observed for g , d , u and s . Finally, the off-diagonal elements show that quark and gluon distributions are instead very mildly correlated to lepton and photon PDFs. Similar results are obtained also for the other configurations.

3 Phenomenological impact

3.1 Parton luminosities

In the computation of the cross sections of hadron-collider processes, PDF contributions factorise in the form of *parton luminosities*. Thus, before looking at specific processes, it is useful to study the behaviour of the parton luminosities of the different initial states, by including also leptons.

Parton luminosities are doubly differential quantities defined as:

$$\frac{d^2 \mathcal{L}_{ij}}{dy d\tau} = f_i(x_1, Q) f_j(x_2, Q), \quad x_1 \equiv \sqrt{\tau} e^y, \quad x_2 \equiv \sqrt{\tau} e^{-y}, \quad \tau \equiv M_X^2/s, \quad (3.1)$$

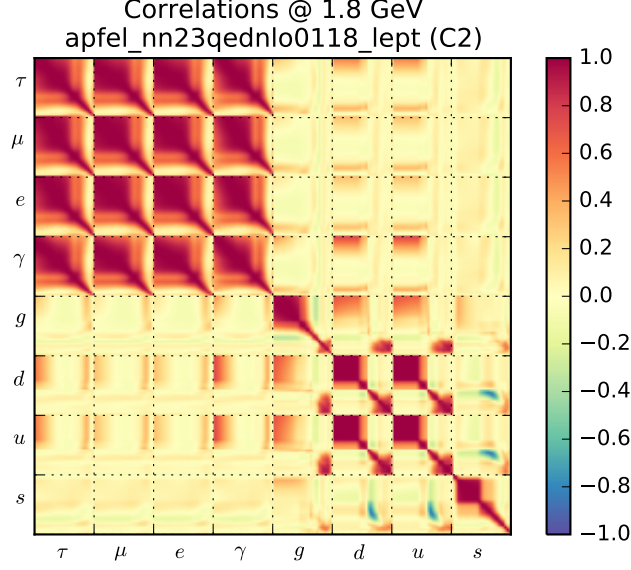


Figure 8: PDF correlation coefficients at $Q = 1.8$ GeV for the configuration C2.

where s is the squared center-of-mass energy of the hadronic collision, and M_X and y are the invariant mass and the rapidity of the partonic initial/final state, respectively. In Eq. (3.1), $f_i(x, Q)$ is the PDF of the i -th parton evaluated at the factorisation scale Q . Different choices for Q can be adopted in order to improve predictions of a particular process and/or distribution. At the level of pure luminosities, without the convolution with any specific matrix element, the factorisation scale can be naturally set to $Q = M_X$.

For the numerical evaluation of the different luminosities, it is practical to integrate out one of the kinematic variables in Eq. (3.1), namely, either τ or y . In particular, by integrating out y , one obtains the M_X -differential luminosities, which read:

$$\Phi_{ij}(M_X) \equiv \frac{d\mathcal{L}_{ij}}{dM_X^2} = \frac{1}{s} \int_{\tau}^1 \frac{dx}{x} f_i(x, M_X) f_j(\tau/x, M_X). \quad (3.2)$$

By integrating out τ , instead, the y -differential luminosities are given by:

$$\Psi_{ij}(y) \equiv \frac{d\mathcal{L}_{ij}}{dy} = 2e^{-2y} \int_{\sqrt{\tau_{\text{cut}}}e^y}^{e^{-y}} dx x f_i(x, \sqrt{s}xe^{-y}) f_j(xe^{-2y}, \sqrt{s}xe^{-y}), \quad (3.3)$$

with $\tau_{\text{cut}} \equiv M_{X,\text{cut}}^2/s$. In Eq. (3.3) the lower bound of the integral, proportional to $\sqrt{\tau_{\text{cut}}}$, implies that $M_X \geq M_{X,\text{cut}}$. Although artificial, this kind of cut is always present in phenomenological predictions. Indeed, in the computation of hadronic cross sections a cut on M_X is automatically introduced by the masses of the particles in the final state or, indirectly, by the cuts on the massless particles, which are necessary to avoid infrared and collinear divergencies and ensure the finiteness of the cross sections.

In order to compare the size and the M_X -dependence of the different parton luminosities, in Fig. 9 we plot $\Phi_{\gamma\gamma}$, $\Phi_{\gamma\ell}$, $\Phi_{\ell^+\ell^-}$, $\Phi_{\ell q}$, $\Phi_{\gamma q}$, $\Phi_{\gamma g}$, $\Phi_{q\bar{q}}$, Φ_{gq} and Φ_{gg} as functions of

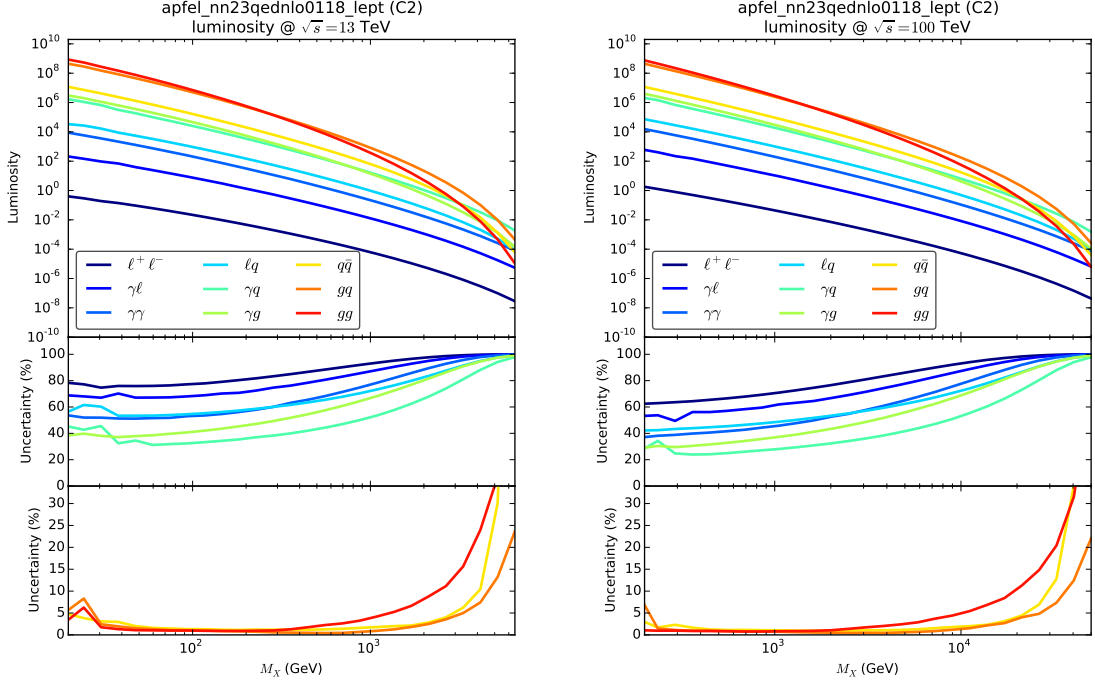


Figure 9: M_X -differential parton luminosities involving also photon and lepton PDFs.

M_X at $\sqrt{s} = 13$ TeV (left) and $\sqrt{s} = 100$ TeV (right) for the set C2. The quantities $\Phi_{i\ell}$, $\Phi_{\ell+\ell^-}$, Φ_{iq} and $\Phi_{q\bar{q}}$ are defined as:

$$\Phi_{i\ell}(M_X) \equiv \sum_{j=e^\pm, \mu^\pm, \tau^\pm} \Phi_{ij}(M_X), \quad \Phi_{\ell+\ell^-}(M_X) \equiv \sum_{j=e, \mu, \tau} \Phi_{j+j^-}(M_X), \quad (3.4)$$

$$\Phi_{iq}(M_X) \equiv \sum_{j=u, \bar{u}, \dots, b, \bar{b}} \Phi_{ij}(M_X), \quad \Phi_{q\bar{q}}(M_X) \equiv \sum_{j=u, d, c, s, b} \Phi_{j\bar{j}}(M_X). \quad (3.5)$$

Similarly, in Fig. 10 we plot the $\Psi_{\gamma\gamma}$, $\Psi_{\gamma\ell}$, $\Psi_{\ell+\ell^-}$, $\Psi_{\ell q}$, $\Psi_{\gamma q}$, $\Psi_{\gamma g}$, $\Psi_{q\bar{q}}$, Ψ_{gq} and Ψ_{gg} parton luminosities as functions of y at the same energies and for the same PDF set. In the case of $\sqrt{s} = 13$ TeV (left), we set $M_{X,\text{cut}} = 10$ GeV and for $\sqrt{s} = 100$ TeV (right) we set $M_{X,\text{cut}} = 100$ GeV. The $\Psi_{i\ell}$, $\Psi_{\ell+\ell^-}$, Ψ_{iq} and $\Psi_{q\bar{q}}$ luminosities are defined in full analogy with Eqs. (3.4) and (3.5). In Figs. 9 and 10 we also plot with consistent colours the 68% uncertainty of the luminosities involving photon or lepton PDFs (lower insets) and of the luminosities involving only (anti)quarks or gluons (central insets).

The relative size of the plotted luminosities follows the expected pattern. In general, the photon PDF suppresses the luminosity by a factor of α w.r.t. the (anti)quark PDFs and, analogously, the lepton PDFs suppress the luminosity by an additional factor of α w.r.t. the photon PDF. This can be easily seen in Fig. 9(10), *e.g.* by comparing $\Phi_{\gamma\ell}(\Psi_{\gamma\ell})$ with $\Phi_{\gamma\gamma}(\Psi_{\gamma\gamma})$ and $\Phi_{\ell+\ell^-}(\Psi_{\ell+\ell^-})$, the three lowest curves. However, from Fig. 9 we also notice that this hierarchy is not clearly respected at large invariant masses. In this kinematic

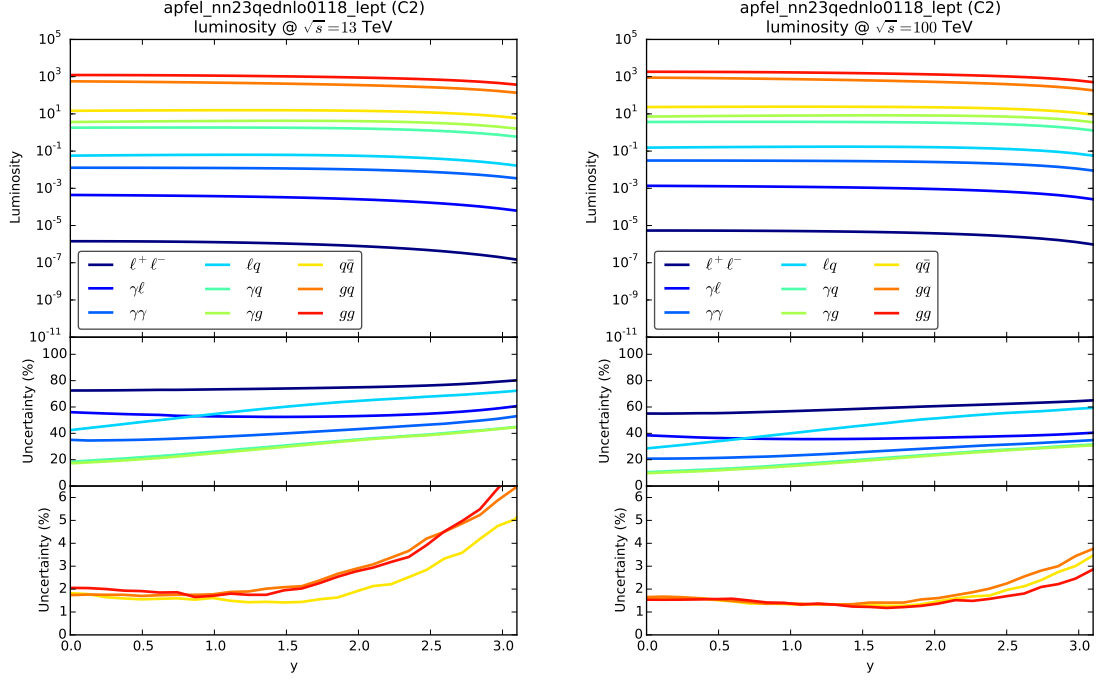


Figure 10: y -differential parton luminosities involving also photon and lepton PDFs.

region the QCD luminosity combinations, $\Phi_{q\bar{q}}$, Φ_{gq} and Φ_{gg} , get closer to the luminosities involving photons and leptons, suggesting possibly non-negligible phenomenological implications due to lepton and photon channels. The major part of this effect is caused by the relative behaviour of the strong coupling α_s with respect to the QED coupling α as functions of the scale M_X . As is well known, DGLAP evolution leads to an increase of PDFs in the small- x region and to a decrease in the large- x region as the evolution scale increases. The magnitude of such a behavior is driven by the rate of change of the coupling, no matter whether it is negative, as for α_s , or positive, as for α . Given that the absolute value of the QCD β -function is larger than the QED one up to very large scales, α_s -driven PDFs, like quark and gluon PDFs, are relatively more suppressed at larger values of x as compared to α -driven PDFs, like lepton and photon PDFs. It is clear from Eq. (3.2) that the behavior of the M_X -differential luminosities at large values of M_X reflects the behavior of PDFs at large values of x and thus, following the argument given above, QCD luminosities are more suppressed than QED luminosities in this region and eventually they get overcome. On the other hand, it should be noticed that in this region the PDF uncertainty for the QED-induced channels is almost as large as the luminosity central value, as shown in the second inset of the plots in Fig. 9. Thus, by taking into account PDF uncertainties, QED luminosities turn out to be compatible at high M_X with QCD luminosities. This feature again points to the fact that meaningful comparisons can be pursued only including PDF errors, especially when those are large, which is in general true for photon and lepton PDFs.

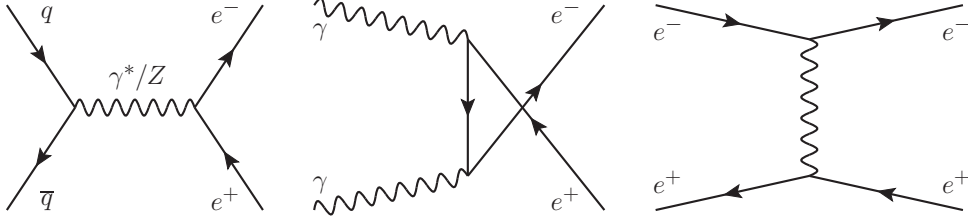


Figure 11: Representative diagrams for partonic processes in e^+e^- production.

Finally, contrary to the Φ_{ij} luminosities, the Ψ_{ij} luminosities maintain the same hierarchy all over the range in y . Indeed, the value of y is not directly related to the value of M_X , which also in this case is used as factorization scale. Thus, the entire previous argument on the suppression of the QCD luminosities with respect to the QED ones does not apply for the case of Ψ_{ij} .

In Fig. 9 the value of M_X on the x -axis have been chosen in such a way that similar values of τ are spanned in the plots for $\sqrt{s} = 13$ TeV and $\sqrt{s} = 100$ TeV. For this reason the curves look very similar in the two plots. The only differences are the size of the 68% uncertainties, which are larger in the 13 TeV case. This effect is due to the different values of the factorisation scale (M_X) for the same values of τ , leading to smaller uncertainties at 100 TeV, where M_X is larger. As expected, PDF uncertainties are much smaller for the QCD initial states (lower inset) than for those involving photons and leptons (central inset).

Similar arguments hold for the comparison of the plot at $\sqrt{s} = 13$ TeV and $\sqrt{s} = 100$ in Fig. 10. Also in this case the values of $M_{X,\text{cut}}$, and consequently of τ_{cut} , have been chosen in such a way that similar values of τ are integrated out in the two cases. With higher values of $M_{X,\text{cut}}$ the difference among the luminosities and even their hierarchy can change, consistently with what is shown in plots of Fig. 9. However, even for large values of $M_{X,\text{cut}}$, partonic luminosities depend very mildly on y .

3.2 Production processes

We now turn to study the effect of lepton PDFs on some key processes at the 13 TeV LHC and at the 100 TeV FCC-hh. The analysis of the parton luminosities presented in Section 3.1 points to a dependence of the relative size of different parton luminosities on the invariant mass of the final-state particles. For this reason, we concentrate on differential distributions w.r.t. this kinematic variable.

All the results have been produced with the help of MADGRAPH5_AMC@NLO [22] using the PDF set C2 in Tab. 1, *i.e.* `apfel_nn23qednlo0118_lept`. The relevant SM input parameters have been set to the following values:

$$\begin{aligned} \alpha_s(m_Z) &= 0.118, & G_F &= 1.16639 \times 10^{-5}, & m_Z &= 91.1876 \text{ GeV}, & m_W &= 80.385 \text{ GeV}, \\ m_H &= 125 \text{ GeV}, & \Gamma_Z &= 2.4952 \text{ GeV}, & \Gamma_W &= 2.085 \text{ GeV}. \end{aligned} \quad (3.6)$$

Since all leptons and quarks, besides the top quark, are considered as partons, they are all treated as massless. As a general approach, for all processes we set renormalisation and

factorisation scales as $\mu_F = \mu_R = H_T/2$, where H_T is the scalar sum of the transverse masses $m_T(i)$ of the final-state particles, defined as:

$$m_T(i) = \sqrt{m(i)^2 + p_T(i)^2}. \quad (3.7)$$

For the sake of simplicity, all simulations are done at LO and parton level. However, we include all the contributions induced by tree-level diagrams, *i.e.* not only those featuring the largest power of α_s but also the subleading contributions. Examples will be given for the specific processes.

We remark that here we focus on the impact of the lepton PDFs at the LHC and at the FCC-hh. In order to perform a trustworthy similar study for the case of the photon PDF, NLO EW corrections cannot be neglected. Notable examples can be found in the context of the SM, *e.g.* in Ref. [23] for the neutral current Drell-Yan or in Ref. [24] for WW production, but also in the context of BSM in Ref. [25] for squark-antisquark production. Nevertheless, in the following, in order to assess the impact of lepton and photon PDFs, we will present results also for photon-induced processes. In general, we will keep separated the contributions from initial states with only (anti)quarks and gluons, initial states with at least one photon and no leptons, and initial states with at least one lepton. In all the plots of this section these three categories are easily identifiable by their distinctive colours, which are red, green and blue respectively.

Neutral Drell-Yan

We start by considering the case of the production of an electron-positron pair at the LHC and at the FCC-hh. Besides the quark-antiquark and photon-photon initial states, this process receives, for instance, a new contribution from the electron-positron initial state, as can be seen in Fig. 11. Similarly, also $\mu^+\mu^-$ and $\tau^+\tau^-$ initial states can contribute. Fig. 11 suggests that different kinematical distributions can arise from different partonic channels such as $q\bar{q}$, with only an s -channel diagram, $\gamma\gamma$, with t - and u -channel diagrams, and e^+e^- with s - and t -channel diagrams. It is important to note that all these partonic processes yield LO cross sections of $\mathcal{O}(\alpha^2)$, thus they all contribute to the same perturbative order.

In Fig. 12 we show the invariant mass distribution of the lepton pair in neutral Drell-Yan production at the 13 TeV LHC, with the following cuts:

$$p_T(e^\pm) > 10 \text{ GeV}, \quad |\eta(e^\pm)| < 2.5. \quad (3.8)$$

In particular, we consider two invariant mass regions: the low invariant mass region, $m(e^+e^-) \in [20 \text{ GeV}, 120 \text{ GeV}]$ and the large invariant mass region $m(e^+e^-) > 1 \text{ TeV}$, shown in the left and right plot, respectively. In the main panel the $q\bar{q}$, $\gamma\gamma$ and $\ell^+\ell^-$ contributions are separately displayed with red, green and blue lines, respectively. Similarly, the black line is the hadronic cross section, *i.e.* the sum of the blue, green and red lines. The bands displayed around each contribution correspond to the PDF uncertainty at 68% CL. In both the high and low invariant-mass regions we find the contribution of initial-state leptons to be fully negligible with respect to the main $q\bar{q}$ one, with a suppression of more than six and

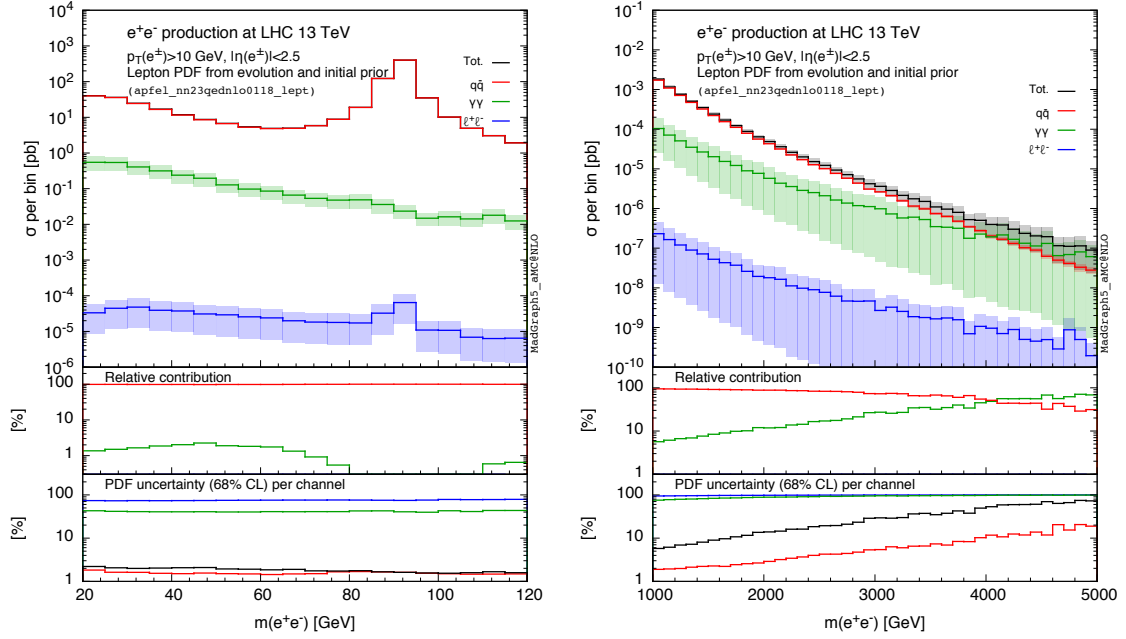


Figure 12: e^+e^- production at the LHC. Low invariant mass (left) and high invariant mass (right) of the lepton pair.

more than two orders of magnitude, respectively. As expected, photon-induced processes are not negligible for large values of $m(e^+e^-)$. This can be seen also in the first inset of the two plots, which display the relative contribution to the hadronic cross section for each of the three channels, with $\ell^+\ell^-$ too small to be visible in the $[1\%, 100\%]$ range. In the third inset we display the relative size of the 68% PDF uncertainty band for the three separate channels and for the hadronic cross section. The $\gamma\gamma$ and $\ell^+\ell^-$ channels entail much larger PDF uncertainties than $q\bar{q}$, however the PDF uncertainty of the hadronic cross section degrades only at large values of $m(\ell^+\ell^-)$ due to the $\gamma\gamma$ contribution.

In Fig. 13 we show similar plots at the 100 TeV FCC-hh for very large invariant masses, $m(e^+e^-) > 5$ TeV. In this case, we also investigate how the results would change by loosening the selection cuts down to values that are presumably not achievable at the experimental level. In the first row of plots in Fig. 13, we apply only the cuts $p_T(e^\pm) > 10$ GeV (left plot) and $p_T(e^\pm) > 100$ GeV (right plot). In both plots the contribution of the $\ell^+\ell^-$ channel is not negligible and in the left plot, for $m(e^+e^-) > 10$ TeV, it is even dominant. This behaviour is due to the $e^+e^- \rightarrow e^+e^-$ partonic cross section with massless electrons, which diverges for electrons collinear to the beam pipe. However, once a reasonable cut $|\eta(e^\pm)| < 4$ on the lepton pseudorapidity is set, the contribution of the $\ell^+\ell^-$ initial state is strongly suppressed. The corresponding distributions with $|\eta(e^\pm)| < 4$ are shown in the lower plots of Fig. 13, again with $p_T(e^\pm) > 10$ GeV (left plot) and $p_T(e^\pm) > 100$ GeV (right plot). In conclusion, although there are kinematic configurations where $\ell^+\ell^-$ initial states are relevant, they are presumably excluded by standard experimental cuts. We observed a similar feature in the $p_T(\ell)$ distributions with $m(e^+e^-) > 2$ TeV at

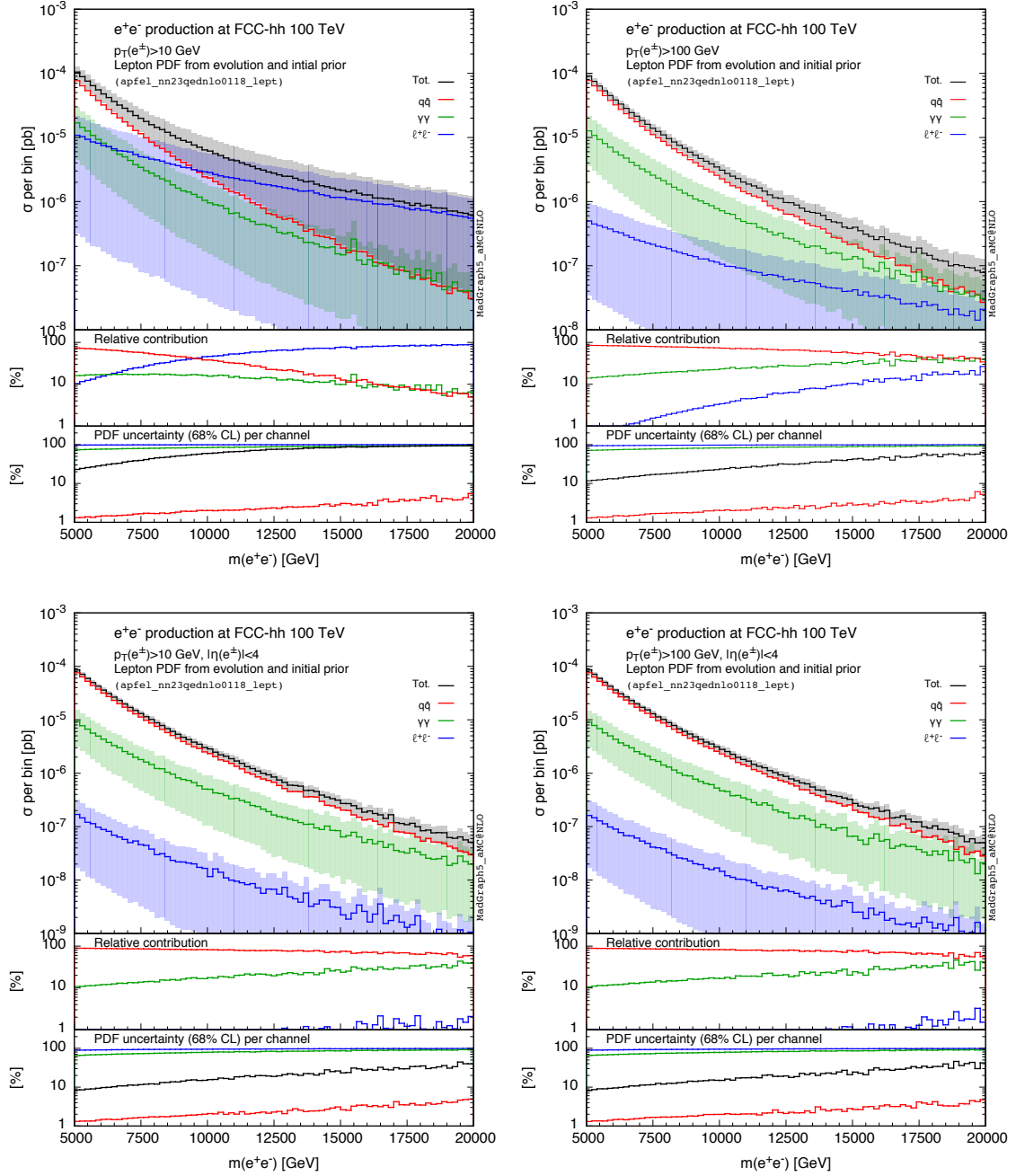


Figure 13: e^+e^- production at the FCC-hh for very high invariant masses with a $p_T > 10$ GeV cut (left column), a $p_T > 100$ GeV cut (right column), without (top row) and with (bottom row) the $|\eta(e^\pm)| < 4$ cut.

the LHC; at small p_T 's the $\ell^+\ell^-$ contribution is dominant, but it is completely suppressed if a cut on $\eta(e^\pm)$ is imposed. For the $\gamma\gamma$ initial state, a detailed analysis of the impact of the PDF uncertainties at differential level has been performed in Ref. [23].

Dijet

The next process we consider is dijet production, the dominant process at hadron colliders. We look at dijet invariant mass ($m(jj)$) distributions, for jets with $p_T(j) > 10(100)$ GeV at the LHC (FCC-hh) and with or without a cut on the jet pseudo-rapidity ($|\eta(j)| < 4$) for the FCC-hh. At the LHC, instead, we always apply the pseudorapidity cut $|\eta(j)| < 2.5$. We consider two cases: in the first we assume zero probability for leptons and photons to fake final state jets, while in second we assume such a probability to be 100%. In other words, in the latter case we consider leptons and photons in the final state on the same footing of quarks and gluons. The realistic value of the fake rate depends on the identity of the particle and on the detector characteristics. At LHC experiments it is typically negligible for photons, electrons and muons, while for taus it is about 40%, see e.g. Ref. [26]. Moreover, the value of the fake rate is also analysis dependent. Thus, by presenting results for the two extreme cases, we provide a conservative estimate of possible effects coming from leptons in the initial state.

Since we consider $2 \rightarrow 2$ processes at LO and parton level, the cut on the transverse momentum of the final state particles is sufficient to obtain a finite cross section and each parton leads to one jet.

We start by showing plots for the first case (no photons/leptons faking jets), in the low and high dijet invariant-mass regions at the LHC and in the very high invariant-mass region at the FCC-hh with and without the $|\eta(j)| < 4$ cut. The LHC and FCC-hh plots are shown in Fig. 14 and Fig. 15. In both cases the lepton-initiated contribution is suppressed by several orders of magnitude. However, part of the suppression does not originate from the PDFs, but from the different perturbative orders of the various partonic channels. The gluon–gluon initial state yields $\mathcal{O}(\alpha_s^2)$ terms, which are the dominant ones at LO, while for instance the photon–gluon and lepton–lepton initial states yield only $\mathcal{O}(\alpha_s\alpha)$ and $\mathcal{O}(\alpha^2)$ contributions, respectively. Therefore, the total rates of these subprocesses are suppressed also by the subleading order in the perturbative expansion. It is worth mentioning that quark–antiquark initial states lead to contributions of $\mathcal{O}(\alpha_s^2)$, $\mathcal{O}(\alpha_s\alpha)$ and $\mathcal{O}(\alpha^2)$, which we consistently take into account in our analysis.

The second case, in which we assume that photons and leptons in the final state are always reconstructed as jets, is particularly interesting because of new t -channel diagrams appearing, *e.g.*, in the $\ell^+\ell^-$ initial state. In general, all the ℓq , $\ell\gamma$ or $\ell_1^\pm\ell_2^\pm$ initial states give a contribution. The relevant plots for the LHC and the FCC-hh are displayed in Fig. 16 and Fig. 17, respectively. Assuming 100% probability for leptons and photons to fake final-state jets, the contributions from initial states with at least one lepton (ℓx) are enhanced in such a way that they become as important as those involving photons and no leptons. However, both contributions are suppressed by at least four orders of magnitude w.r.t. those initiated by QCD partons.

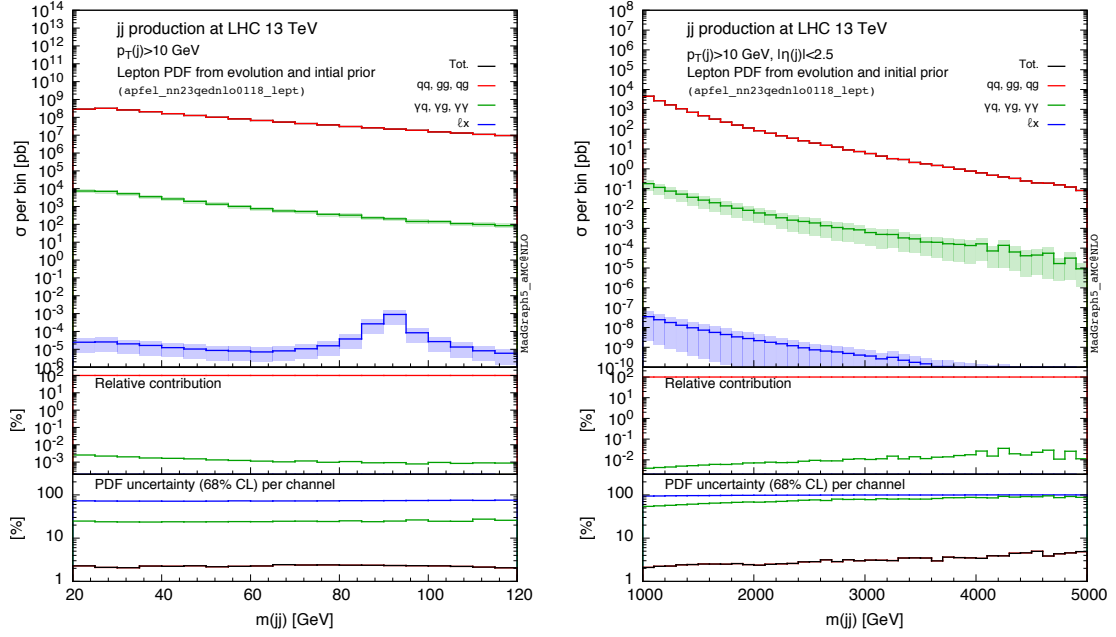


Figure 14: Dijet production at the LHC. Low (left) and high (right) invariant mass of the dijet pair. Zero probability of photons/leptons faking jets is assumed.

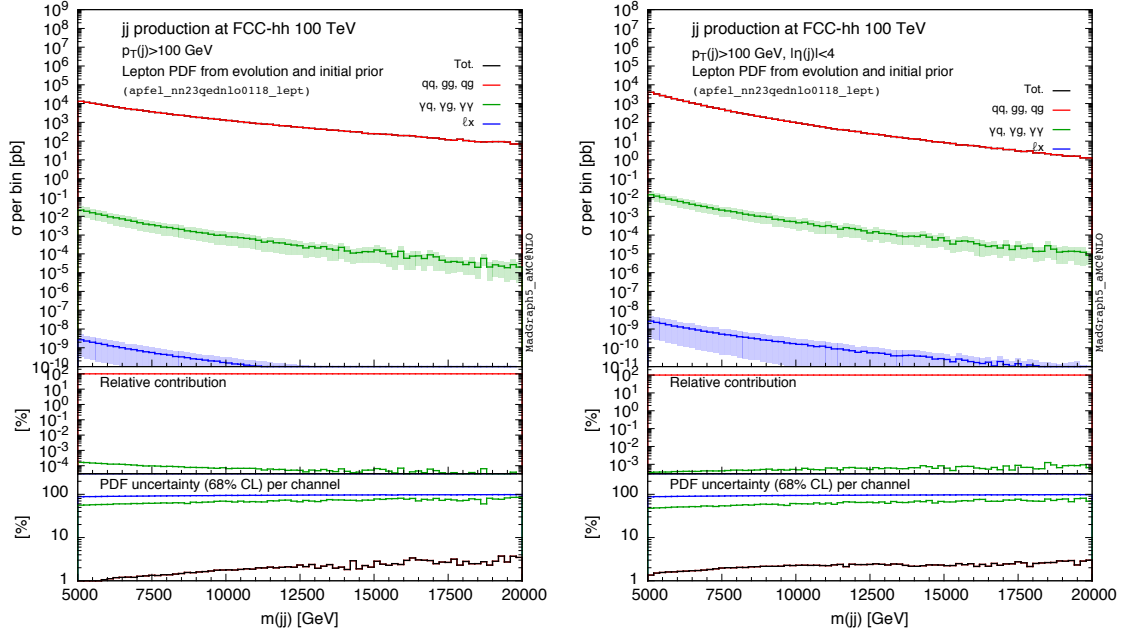


Figure 15: Dijet production at the FCC-hh in the very-high invariant mass region, without (left) or with (right) the $|\eta(j)| < 4$ cut. Zero probability of photons/leptons faking jets is assumed.

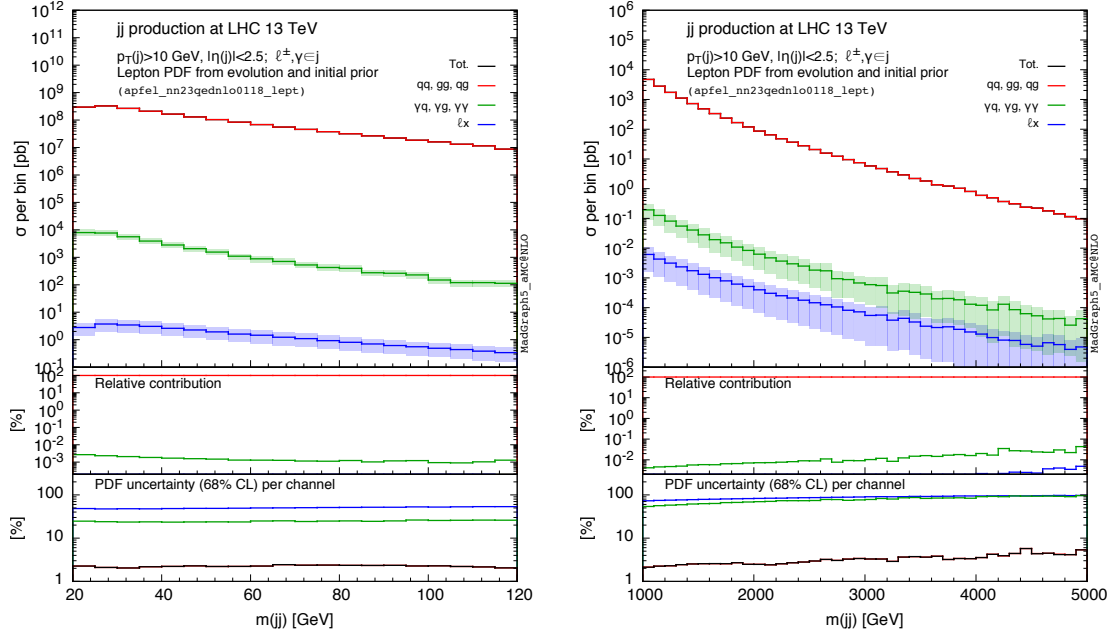


Figure 16: Dijet production at the LHC in the low (left) and high(right) invariant mass region. 100% probability of photons/leptons faking jets is assumed.

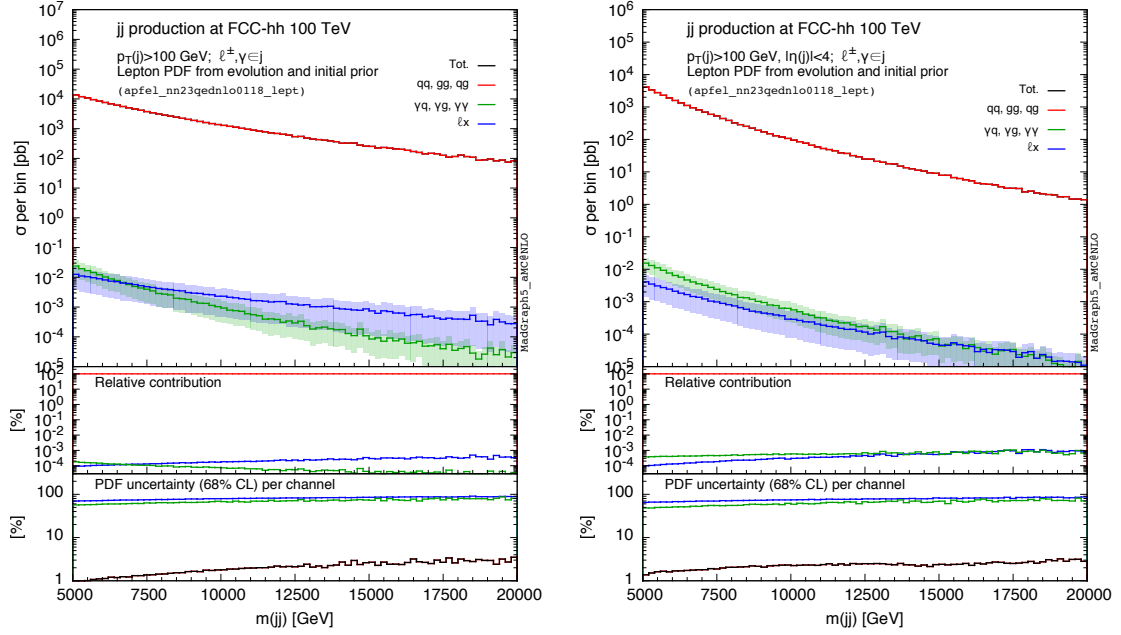


Figure 17: Dijet production at the FCC-hh in the very-high invariant mass region, without (left) or with (right) the $|\eta(j)| < 4$ cut. 100% probability of photons/leptons faking jets is assumed.

W^+W^- and ZZ into 4 leptons

Next we turn to diboson production at hadron colliders. Firstly, we look at W^+W^- production with undecayed W bosons. Then we analyse four-lepton production which is the signature emerging from ZZ production with both Z bosons decaying into two leptons.

In the case of W^+W^- production, we keep the W boson stable so that we can gauge the effects due only to the $\ell^+\ell^-$ luminosity and not to matrix-element enhancements. The latter effects will be instead analysed in the case of ZZ production. Moreover, with stable W bosons, it is possible to check if any effect from lepton PDFs could be related to the anomaly that has been recently found by the ATLAS Collaboration in the production of dibosons with 2 TeV invariant mass in the Run-I of the LHC [27].

Differential distributions for the invariant mass $m(W^+W^-)$ of the W^+W^- pair are shown in Fig. 18, for the LHC in the upper plots and for the FCC-hh in the lower plots. For both colliders we consider the case without cuts (plots on the left) and with $|\eta(W^\pm)| < 2.5(4)$ at the LHC (FCC-hh) (plots on the right). Also for this process the lepton PDF contribution can be in general safely neglected. On the contrary, the photon-induced processes have to be taken into account for a reliable estimate of the central value of the cross section and the associated uncertainty due to PDFs in the large invariant-mass region. A similar study at the LHC, including NLO QCD and EW corrections but with no PDF uncertainty, have been pursued also in Ref. [24]. The increase of the relative size of the $\gamma\gamma$ -channel for high $m(W^+W^-)$ is consistent with the behaviour of the $\Phi_{\gamma\gamma}$ and $\Phi_{q\bar{q}}$ luminosities shown in Fig. 9. In addition, no suppression from s -channel diagrams is present in $\gamma\gamma \rightarrow W^+W^-$ production, leading to a further relative enhancement with respect to the $q\bar{q}$ -channel at high $m(W^+W^-)$. On the other hand, in the $\gamma\gamma$ -channel the W bosons are produced more peripherally than in the $q\bar{q}$ -channel. Thus, the cut in pseudorapidity reduces the relative impact of the $\gamma\gamma$ channel, but it does not dramatically change the qualitative picture.

In the case of ZZ production, we analyse the four-lepton final state emerging from the decay of the Z bosons. Specifically, we consider either four leptons of the same flavour ($e^+e^-e^+e^-$), or two lepton pairs of different flavours ($e^+e^-\mu^+\mu^-$). All diagrams, with and without intermediate Z bosons, are taken into account. Thus, all the resonant and non-resonant contributions have been properly included. It is worth noting that, if we were requiring stable Z bosons, no $\gamma\gamma$ -initiated contribution would appear, since the process $\gamma\gamma \rightarrow ZZ$ has no tree-level diagrams. Moreover, as in the case of neutral Drell-Yan, final-state leptons collinear to the beam axis lead to divergent cross sections for the $\ell^+\ell^-$ channel.

In Figs. 19 and 20 we show differential distributions for the invariant mass of the four-lepton system at the LHC and FCC-hh, respectively. In our simulations at the LHC we required four leptons with:

$$p_T(\ell) > 10 \text{ GeV}, \quad |\eta(\ell)| < 2.5, \quad (3.9)$$

while at the FCC-hh they must satisfy:

$$p_T(\ell) > 100 \text{ GeV}, \quad |\eta(\ell)| < 4. \quad (3.10)$$

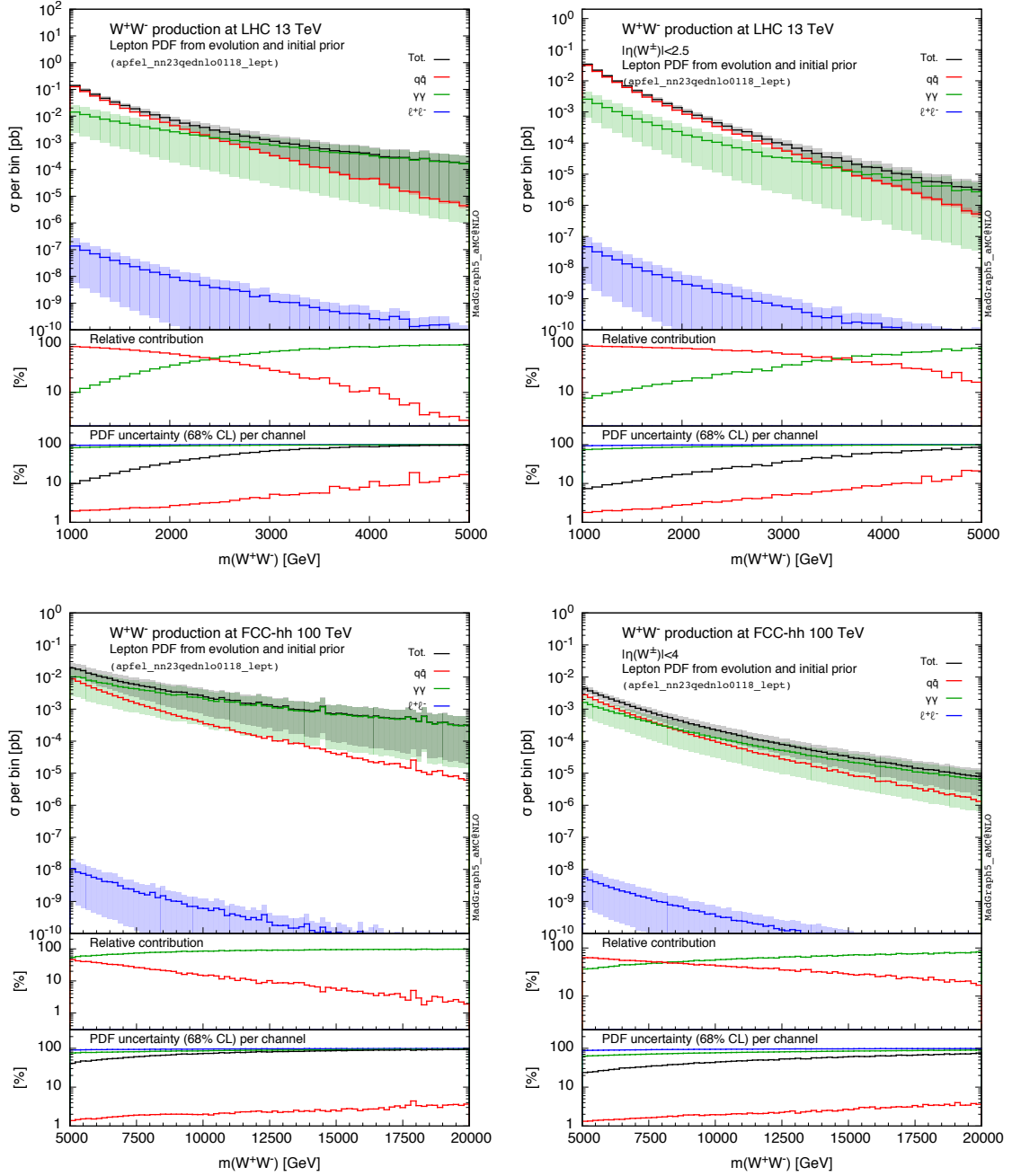


Figure 18: W pair production at the LHC (top row) and at the FCC-hh (bottom row), both without cuts (left column) or with a rapidity cut (right column). The rapidity cut is $|\eta(W^\pm)| < 2.5(4)$ at the LHC (FCC-hh).

Furthermore, we require that all opposite-sign lepton pairs have an invariant mass $m(\ell^\pm, \ell'^\mp) > 20$ GeV to avoid collinear singularities due to photon splittings. Again, we clearly observe that the $\ell^+\ell^-$ -initiated contribution is completely negligible. The largest relative contribution to the cross section is at most at the per-mil level at very large values of the four-lepton

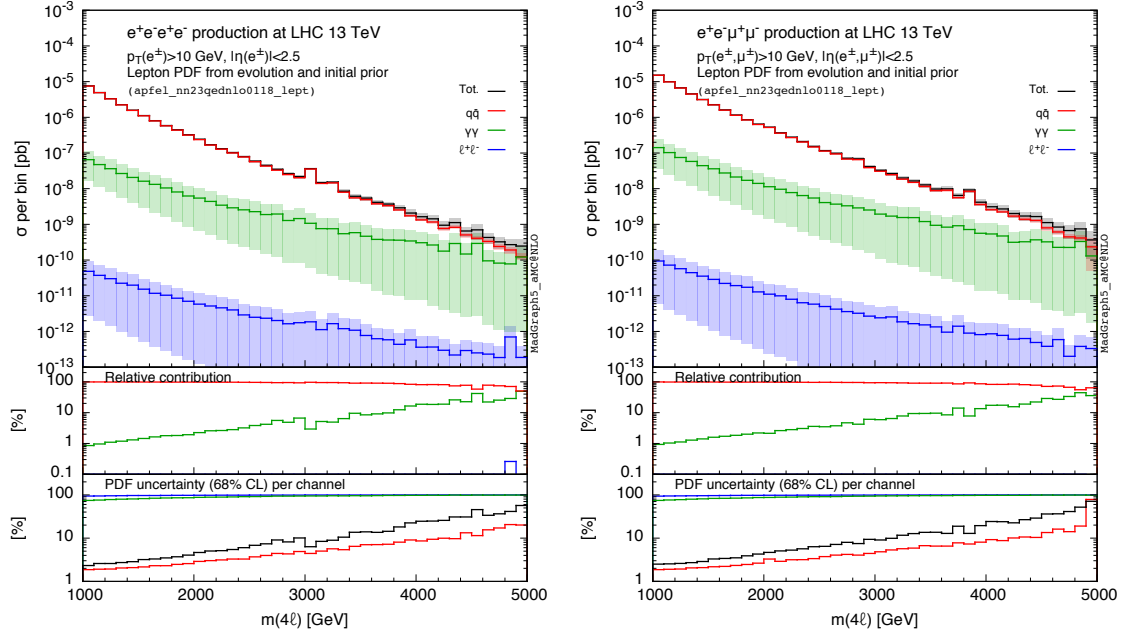


Figure 19: Four lepton production at the LHC: the case of all four leptons of the same flavour (left) and of two different flavour pairs (right) is considered.

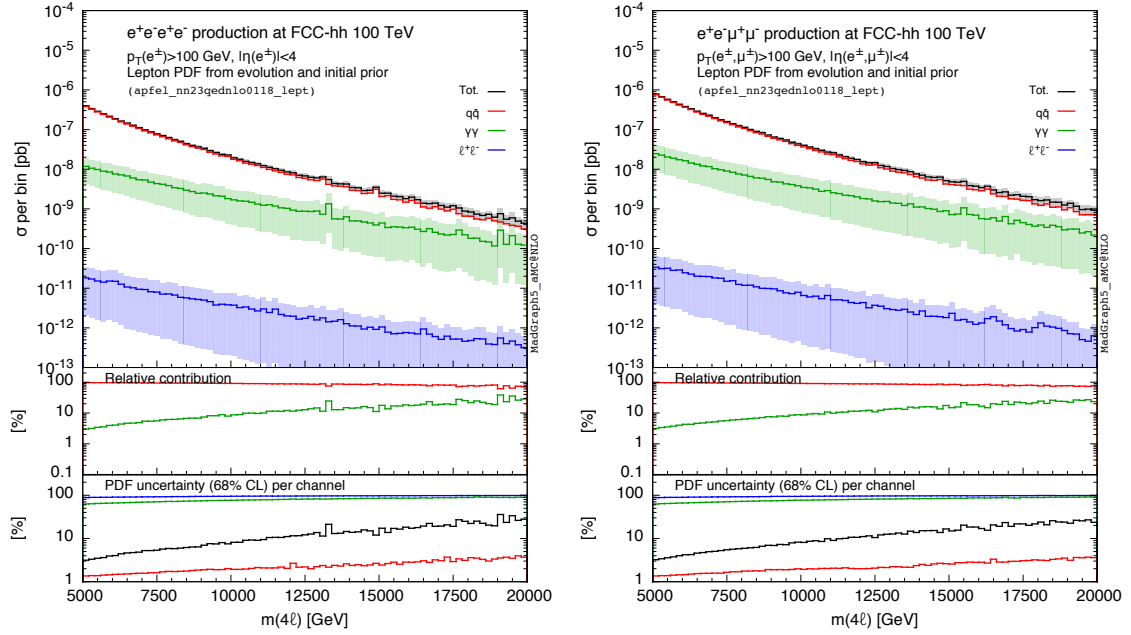


Figure 20: Four lepton production at the FCC-hh: the case of all four leptons of the same flavour (left) and of two different flavour pairs (right) is considered.

invariant mass and tends to become even smaller in the lower invariant-mass region.

Same-Sign and/or Different-Flavour lepton pair

We conclude our review of SM processes discussing two cases which are relevant for both SM physics and BSM searches: the production of a same-sign lepton pair and of a different-flavour lepton pair. For such searches in the BSM context, the SM background processes that are typically considered are those featuring two vector bosons in the final state (ZZ , WZ , $W^\pm W^\pm jj$, $W^\pm W^\mp$, $t\bar{t} \rightarrow W^\pm W^\mp b\bar{b}$, ...), where the same-sign/different-flavour pair of leptons comes together with jets, other (undetected) leptons and/or missing transverse energy. Therefore it is worth estimating the lepton-initiated contribution to the SM background for these processes.

Before presenting our results, we want to stress one important fact to be kept in mind: the introduction of lepton PDFs does not open new production mechanisms. Rather, it has to be considered as a different scheme to tackle a given computation, on the same footing as the four- and five-flavour schemes in processes involving bottom quarks. For example, the process $e^+e^+ \rightarrow e^+e^+$, computed with lepton PDFs, corresponds to the process $\gamma\gamma \rightarrow e^+e^-e^+e^-$ where leptons are considered as *massive* and the e^- degrees of freedom are integrated out. This latter scheme has several drawbacks if compared to the one with leptons in the initial state: first, the process has a larger final-state multiplicity and is therefore more challenging from the computational point of view. On top of this, lepton masses are very small as compared to the typical scales probed at the LHC and FCC-hh. As a consequence, the numerical evaluation and integration of matrix elements can be hampered by instabilities. In particular, large logarithms of the form $\alpha \log(Q/m_\ell)$, where Q is a typical hard scale of the hadronic process, could spoil the convergence of the numerical integration. On the contrary, using lepton PDFs, such logarithms are analytically taken into account from m_ℓ up to Q_0 by the initial condition in Eq. (2.6) and consistently resummed from Q_0 to Q by DGLAP evolution. Therefore, the usage of a scheme with lepton PDFs simplifies the computation, and consequently the phenomenological studies, for the classes of processes considered here.

After this clarification, we start by considering the same-sign lepton-pair production. We compare the $\ell^+\ell^+$ -initiated case to the process $qq \rightarrow W^\pm W^\pm qq$, where both the W bosons decay leptonically. For this process, which has also been proposed as a way to search for and calibrate double-parton scattering at the LHC [28], we do not need to consider additional untagged leptons and the cross section is finite even without cuts on jets.

We quote total rates for $qq \rightarrow W^+W^+qq \rightarrow \ell^+\ell^+\nu_\ell\nu_\ell qq$ and for $\ell^+\ell^+ \rightarrow \ell^+\ell^+$ in Tab. 2. For the former, we include all coupling combinations entering at LO, *i.e.* we evaluate this process at the orders $|\alpha_s\alpha^2 + \alpha^3|^2$.² As usual, we consider the case of the LHC and of the FCC-hh, requiring the two charged leptons to satisfy the cuts of Eqs. (3.9) and (3.10), respectively. We can see that in this case the lepton-initiated contribution is not entirely negligible as compared to the same-sign W pair production rate, at least at the LHC. In this case, the former contribution is 7% of the latter, while this ratio reduces to 1% at the

² In Ref. [28] it is shown that the electroweak contribution to the cross section is of the same order of magnitude of the QCD one. Thus, it cannot be ignored.

$\ell = e, \mu, \tau$	LHC, $\sigma[\text{pb}]$	FCC-hh, $\sigma[\text{pb}]$
$qq \rightarrow \ell^+ \ell^+ \nu \nu jj$	$3.54 \cdot 10^{-2} \pm 0.4\%$	$6.33 \cdot 10^{-2} \pm 0.3\%$
$\ell^+ \ell^+ \rightarrow \ell^+ \ell^+$	$2.64 \cdot 10^{-3} \pm 37\%$	$5.86 \cdot 10^{-4} \pm 22\%$

Table 2: Rates for same-sign lepton pair production at the LHC and FCC-hh. Leptons are required to satisfy the cuts $p_T > 10(100) \text{ GeV}$, $|\eta| < 2.5(4)$ at the LHC (FCC-hh). Quoted uncertainties are from PDFs, at 68% CL.

	LHC, $\sigma[\text{pb}]$	FCC-hh, $\sigma[\text{pb}]$
$e^+ \mu^- \rightarrow e^+ \mu^-$	$5.35 \cdot 10^{-4} \pm 38\%$	$9.93 \cdot 10^{-5} \pm 22\%$
$e^+ \tau^- \rightarrow e^+ \tau^-$	$5.06 \cdot 10^{-4} \pm 37\%$	$9.65 \cdot 10^{-5} \pm 22\%$
$\tau^+ \mu^- \rightarrow \tau^+ \mu^-$	$4.95 \cdot 10^{-4} \pm 38\%$	$9.46 \cdot 10^{-5} \pm 23\%$
$pp \rightarrow e^+ \mu^- \nu_e \tilde{\nu}_\mu$	$4.90 \cdot 10^{-1} \pm 0.6\%$	$2.01 \cdot 10^{-1} \pm 0.4\%$
$pp \rightarrow e^+ \mu^- \nu_e \tilde{\nu}_\mu, \cancel{E}_T > 20 \text{ GeV}$	$9.96 \cdot 10^{-2} \pm 0.6\%$	$4.27 \cdot 10^{-2} \pm 0.5\%$

Table 3: Rates for different-flavour lepton-pair production at the LHC and FCC-hh. Final-state leptons are required to satisfy the cuts $p_T > 10(100) \text{ GeV}$, $|\eta| < 2.5(4)$ at the LHC (FCC-hh). Quoted uncertainties are from PDFs, at 68% CL.

FCC-hh. In both cases PDF uncertainties affecting the lepton-initiated contribution are quite large. The quoted results are shown for the case of positively charged leptons. In the case of negatively charged leptons, the lepton-initiated cross section does not change, while the cross section for $qq \rightarrow W^- W^- qq$ is reduced by approximately a factor 2 (1.4) with respect to the positively charged case at the LHC (FCC-hh). The quoted numbers include the contributions from all the three leptonic flavours. For $qq \rightarrow W^\pm W^\pm qq$, different-flavour and same-flavour leptons yield two thirds and one third of the total cross section, respectively, due to lepton universality. Instead, for $\ell^\pm \ell^\pm \rightarrow \ell^\pm \ell^\pm$ the relative contributions are 60% and 40% because of non-negligible interference effects that appear only for same-flavour and same-sign lepton pair production.

As far as the case of opposite-sign and different-flavour lepton-pair production is concerned, the total rates for the various flavour combinations are shown in Tab. 3. In the table we show lepton-initiated processes and compare them with a non-lepton-initiated reaction with the same signature, $pp \rightarrow \ell^+ \ell'^- \nu \nu$. Leptons are required to satisfy the same cuts as in the same-sign case, *i.e.* Eqs. (3.9) and (3.10). For what concerns $pp \rightarrow \ell^+ \ell'^- \nu \nu$, besides the cuts on leptons we also study the effect of a cut on the missing transverse energy $\cancel{E}_T < 20 \text{ GeV}$, in order to enhance configurations with the two leptons back-to-back. This cut can be considered realistic for the LHC³, while it may be optimistic at the FCC, for which the precise experimental setup is presently unknown. In all cases, lepton-initiated contributions are suppressed with respect to $pp \rightarrow \ell^+ \ell'^- \nu \nu$, and remain below the 1% level even with the \cancel{E}_T cut.

³ The typical missing transverse energy resolution in events with a low- p_T lepton pair at LHC experiments is 10 GeV or less [29–33]

Slepton pair $\tilde{\ell}\tilde{\ell}^*$

The last case that we analyse is relevant for BSM; we consider the hadroproduction of a slepton pair ($\tilde{\ell}\tilde{\ell}^*$) within the Minimal Supersymmetric Standard Model (MSSM). Again, we are mainly interested in assessing whether contributions initiated by leptons can affect the discovery searches of these particles. Anyway, as done in the previous cases, we consider also photon-initiated processes. A similar and more detailed study for $\gamma\gamma$ initial state has been performed in Ref. [25] for the case of squark-antisquark production, where the $\gamma\gamma$ contribution has been found to be non-negligible. Here, for slepton-antislepton production, we just provide results for total rates. However, at variance with the squark-antisquark case, in slepton-antislepton production $\gamma\gamma$ - as well as $\ell^+\ell^-$ -initiated processes are of the same perturbative order of $q\bar{q}$, *i.e.* $\mathcal{O}(\alpha^2)$. Therefore, we expect a larger relative impact from photon-initiated processes.

In $\tilde{\ell}\tilde{\ell}^*$ production, tree-level Feynman diagrams are very similar to the case of e^+e^- production. The $q\bar{q}$ initial state proceeds via (non-resonant) Drell-Yan production, and the $\gamma\gamma$ initial state presents t - and u -channel diagrams. The $\ell^+\ell^-$ initial state proceeds via both Drell-Yan production and t -channel neutralino exchange. Also, at variance with the $q\bar{q}$ and $\gamma\gamma$ initial states, at LO the $\ell^+\ell^-$ initial state can produce $\tilde{\ell}_1\tilde{\ell}_2^*$ where both the chirality and the flavour of $\tilde{\ell}_1$ and $\tilde{\ell}_2^*$ are different.

In order to minimise the dependence on the MSSM parameters, we have chosen to consider only the cases $\ell = e, \mu$. In this way we avoid the dependence on the left-right mixing parameters in the stau sector. Moreover, all the particles besides the selectrons, smuons and the lightest neutralino have been decoupled by setting their masses to 5 TeV. The neutralino mixing matrix and the physical masses have been calculated at the scale of the slepton mass $m_{\tilde{\ell}}$, with the help of SUSPECT [34].

In Tab. 4 we list the results for the total cross sections of $\tilde{\ell}\tilde{\ell}^*$ production at the LHC and FCC-hh, where the soft masses for right-handed and left-handed leptons of the first two families have been set to $m_{\tilde{\ell}}=200, 500, 1200$ GeV and the mass of the lightest neutralino to $m_{\tilde{\chi}_1^0}=100$ GeV. Physical masses are slightly different from soft masses, however, the small differences are completely irrelevant for the study pursued here, so we do not report them in the text. The numbers in Tab. 4 refer to the sum of all the possible chirality and flavour configurations. Also for this process, the contribution due to leptons in the initial state is in general negligible. Even setting $m_{\tilde{\chi}_1^0}=1$ GeV, the lepton-lepton contribution results slightly enhanced, but the qualitative picture does not change. Conversely, photon-induced processes are relevant and cannot be neglected at the LHC, especially for large masses.

4 Conclusions and outlook

In this paper we have presented the first-ever estimate of the lepton content of the proton. By implementing the complete LO QED corrections to the DGLAP evolution equations in the APFEL program and by means of a model for the lepton PDFs at the initial scale, we have produced PDF sets in the LHAPDF6 format containing, besides the usual PDFs for quarks and gluons and possibly photons, distributions for all charged leptons. The main result of this work are the sets produced according to the ansatz in Eq. (2.6), *i.e.*

LHC, $\sigma(pp \rightarrow \tilde{\ell}\tilde{\ell}^*)[\text{pb}]$			
Initial state	$m_{\tilde{\ell}} = 200 \text{ GeV}$	$m_{\tilde{\ell}} = 500 \text{ GeV}$	$m_{\tilde{\ell}} = 1200 \text{ GeV}$
Total	$5.24 \cdot 10^{-2} \pm 4\%$	$1.31 \cdot 10^{-3} \pm 10\%$	$1.19 \cdot 10^{-5} \pm 38\%$
$q\bar{q}$	$4.98 \cdot 10^{-2} \pm 1\%$	$1.18 \cdot 10^{-3} \pm 2\%$	$7.52 \cdot 10^{-6} \pm 6\%$
$\gamma\gamma$	$2.62 \cdot 10^{-3} \pm 72\%$	$1.32 \cdot 10^{-4} \pm 84\%$	$4.38 \cdot 10^{-6} \pm 95\%$
$\ell^+\ell^-$	$6.70 \cdot 10^{-7} \pm 92\%$	$4.92 \cdot 10^{-8} \pm 97\%$	$1.68 \cdot 10^{-9} \pm 99\%$

FCC-hh, $\sigma(pp \rightarrow \tilde{\ell}\tilde{\ell}^*)[\text{pb}]$			
Initial state	$m_{\tilde{\ell}} = 200 \text{ GeV}$	$m_{\tilde{\ell}} = 500 \text{ GeV}$	$m_{\tilde{\ell}} = 1200 \text{ GeV}$
Total	$8.42 \cdot 10^{-1} \pm 2\%$	$4.88 \cdot 10^{-2} \pm 3\%$	$2.35 \cdot 10^{-3} \pm 5\%$
$q\bar{q}$	$8.13 \cdot 10^{-1} \pm 1\%$	$4.64 \cdot 10^{-2} \pm 1\%$	$2.19 \cdot 10^{-3} \pm 1\%$
$\gamma\gamma$	$2.94 \cdot 10^{-2} \pm 46\%$	$2.32 \cdot 10^{-3} \pm 52\%$	$1.58 \cdot 10^{-4} \pm 62\%$
$\ell^+\ell^-$	$6.22 \cdot 10^{-6} \pm 74\%$	$8.09 \cdot 10^{-7} \pm 80\%$	$7.86 \cdot 10^{-8} \pm 87\%$

Table 4: Total rates for slepton-pair production at the LHC and at the FCC-hh. Quoted uncertainties refer to PDF uncertainties at the 68% CL.

by assuming that leptons are produced in pairs by photon splitting at the respective mass scales.

By studying the feature of the PDFs, we found that our results are consistent with the expectations. Lepton PDFs are strongly correlated to the photon PDF and suppressed by a factor α w.r.t. it. As a consequence of their small size, their phenomenological impact at hadron colliders is likely to be limited. Also, the uncertainties of lepton PDFs can be very large, as in the case of the photon PDF. We explicitly checked the phenomenological impact of lepton-induced partonic channels for several relevant SM processes at the LHC at 13 TeV and at the 100 TeV FCC-hh. With reasonable experimental cuts, the contributions of lepton PDFs is usually extremely suppressed. On the contrary, the photon PDF contribution is not negligible and has to be carefully studied for precise predictions at the LHC and FCC-hh. We also presented representative results for BSM processes (slepton-antislepton production in the MSSM) and rare SM processes such as same-sign and/or different-flavour dilepton production. More detailed studies, including higher-order effects as well as realistic cuts and background simulations, are envisaged, since the role of the lepton PDFs could be relevant in this context.

The combined QCD+QED evolution with lepton PDFs has been implemented in APFEL version 2.4.0 and later, publicly available at:

<https://github.com/scarrazza/apfel>

The sets of PDFs used in this work, produced with APFEL, are also publicly available in the LHAPDF6 library format from the APFEL webpage⁴:

`apfel_nn23nlo0118_lep0`, `apfel_nn23nnlo0118_lep0`,

⁴<http://apfel.hepforge.org/>

apfel_nn23qedlo0118.lept0, apfel_nn23qednlo0118.lept0, apfel_nn23qednnlo0118.lept0,
 apfel_nn23qedlo0118.lept, apfel_nn23qednlo0118.lept, apfel_nn23qednnlo0118.lept,
 apfel_mrsto4qed.lept0, apfel_mrsto4qed.lept

Acknowledgments

We are grateful to Roberto Salerno, Lorenzo Calibbi, Stefano Frixione, Fabio Maltoni, Michelangelo Mangano, Juan Rojo, Stefano Forte and the MG5_aMC@NLO Collaboration members for fruitful discussions and suggestions during the development of this project.

This work is partially supported by an Italian PRIN2010 grant (S.C.), by a European Investment Bank EIBURS grant (S.C.) and by the ERC grant 291377, LHCtheory: *Theoretical predictions and analyses of LHC physics: advancing the precision frontier* (V.B., S.C. and D.P.). The work of M.Z. is supported by the ERC grant Higgs@LHC and partially by the ILP LABEX (ANR-10-LABX-63), in turn supported by French state funds managed by the ANR within the “Investissements d’Avenir” programme under reference ANR- 11-IDEX-0004-02.

A The combined QCD+QED evolution in the presence of lepton PDFs

The DGLAP evolution equations employed in this work for the unified QCD+QED evolution in the presence of lepton PDFs consist of a system of coupled differential equations which satisfy both QCD and QED evolution equations. In order to simultaneously diagonalise as much as possible the respective evolution matrices, avoiding unnecessary couplings between parton distributions, we have adopted the following evolution basis:

$$\begin{aligned}
 1 : g & & 12 : V = V_u + V_d \\
 2 : \gamma & & 13 : \Delta_V = V_u - V_d \\
 3 : \Sigma = \Sigma_u + \Sigma_d & & 14 : V_\ell \\
 4 : \Delta_\Sigma = \Sigma_u - \Sigma_d & & 15 : V_1^u = u^- - c^- \\
 5 : \Sigma_\ell & & 16 : V_2^u = u^- + c^- - 2t^- \\
 6 : T_1^u = u^+ - c^+ & & 17 : V_1^d = d^- - s^- \\
 7 : T_2^u = u^+ + c^+ - 2t^+ & & 18 : V_2^d = d^- + s^- - 2b^- \\
 8 : T_1^d = d^+ - s^+ & & 19 : V_3^\ell = l_e^- - l_\mu^- \\
 9 : T_2^d = d^+ + s^+ - 2b^+ & & 20 : V_8^\ell = l_e^- + l_\mu^- - 2l_\tau^- \\
 10 : T_3^\ell = l_e^+ - l_\mu^+ & & \\
 11 : T_8^\ell = l_e^+ + l_\mu^+ - 2l_\tau^+ & &
 \end{aligned} \tag{A.1}$$

where we have defined:

$$\begin{aligned}
 q^\pm &= q \pm \bar{q} \quad \text{with } q = u, d, s, c, b, t, \\
 l_\ell^\pm &= \ell^- \pm \ell^+ \quad \text{with } \ell = e, \mu, \tau,
 \end{aligned} \tag{A.2}$$

and:

$$\begin{aligned}
\Sigma_u &= u^+ + c^+ + t^+, & V_u &= u^- + c^- + t^-, \\
\Sigma_d &= d^+ + s^+ + b^+, & V_d &= d^- + s^- + b^-, \\
\Sigma_\ell &= l_e^+ + l_\mu^+ + l_\tau^+, & V_\ell &= l_e^- + l_\mu^- + l_\tau^-.
\end{aligned} \tag{A.3}$$

When considering LO QED corrections to the DGLAP equations, the evolution equations in the basis given in Eq. (A.1) decouple into different sectors that evolve independently as shown below. It should also be noticed that considering only LO QED corrections allows one to completely separate QCD and QED corrections. Indeed, defining \tilde{P} the QCD splitting functions (up to any of the known orders in α_s [35–39]) and $\bar{P} = (\alpha/4\pi)P^{(0)}$ the LO QED splitting functions, with $P^{(0)}$ given in Eq. (2.3), we have:

- the singlet sector:

$$\begin{aligned}
\mu^2 \frac{\partial}{\partial \mu^2} \begin{pmatrix} g \\ \gamma \\ \Sigma \\ \Delta_\Sigma \\ \Sigma_\ell \end{pmatrix} &= \left[\begin{pmatrix} \tilde{P}_{gg} & 0 & \tilde{P}_{gq} & 0 & 0 \\ 0 & 0 & 0 & 0 & 0 \\ 2n_f \tilde{P}_{qg} & 0 & \tilde{P}_{qq} & 0 & 0 \\ \frac{n_u-n_d}{n_f} 2n_f \tilde{P}_{qg} & 0 & \frac{n_u-n_d}{n_f} (\tilde{P}_{qq} - \tilde{P}^+) & \tilde{P}^+ & 0 \\ 0 & 0 & 0 & 0 & 0 \end{pmatrix} \right. \\
&\quad \left. + \begin{pmatrix} 0 & 0 & 0 & 0 & 0 \\ 0 & e_\Sigma^2 \bar{P}_{\gamma\gamma} & \eta^+ \bar{P}_{\gamma q} & \eta^- \bar{P}_{\gamma q} & \bar{P}_{\gamma q} \\ 0 & 2e_\Sigma^2 \bar{P}_{q\gamma} & \eta^+ \bar{P}_{qq} & \eta^- \bar{P}_{qq} & 0 \\ 0 & 2\delta_e^2 \bar{P}_{q\gamma} & \eta^- \bar{P}_{qq} & \eta^+ \bar{P}_{qq} & 0 \\ 0 & 2n_\ell \bar{P}_{q\gamma} & 0 & 0 & \bar{P}_{qq} \end{pmatrix} \right] \otimes \begin{pmatrix} g \\ \gamma \\ \Sigma \\ \Delta_\Sigma \\ \Sigma_\ell \end{pmatrix}, \tag{A.4}
\end{aligned}$$

- the quark valence sector:

$$\mu^2 \frac{\partial}{\partial \mu^2} \begin{pmatrix} V \\ \Delta_V \end{pmatrix} = \left[\begin{pmatrix} \tilde{P}^V & 0 \\ \frac{n_u-n_d}{n_f} (\tilde{P}^V - \tilde{P}^-) & \tilde{P}^- \end{pmatrix} + \begin{pmatrix} \eta^+ \bar{P}_{qq} & \eta^- \bar{P}_{qq} \\ \eta^- \bar{P}_{qq} & \eta^+ \bar{P}_{qq} \end{pmatrix} \right] \otimes \begin{pmatrix} V \\ \Delta_V \end{pmatrix}, \tag{A.5}$$

- the lepton valence sector:

$$\mu^2 \frac{\partial V_\ell}{\partial \mu^2} = \bar{P}_{qq} \otimes V_\ell, \tag{A.6}$$

- the quark non-singlet sector:

$$\begin{aligned}
\mu^2 \frac{\partial T_{1,2}^u}{\partial \mu^2} &= (\tilde{P}^+ + e_u^2 \bar{P}_{qq}) \otimes T_{1,2}^u, \\
\mu^2 \frac{\partial T_{1,2}^d}{\partial \mu^2} &= (\tilde{P}^+ + e_d^2 \bar{P}_{qq}) \otimes T_{1,2}^d, \\
\mu^2 \frac{\partial V_{1,2}^u}{\partial \mu^2} &= (\tilde{P}^- + e_u^2 \bar{P}_{qq}) \otimes V_{1,2}^u, \\
\mu^2 \frac{\partial V_{1,2}^d}{\partial \mu^2} &= (\tilde{P}^- + e_d^2 \bar{P}_{qq}) \otimes V_{1,2}^d,
\end{aligned} \tag{A.7}$$

- and the lepton non-singlet sector:

$$\begin{aligned}
\mu^2 \frac{\partial T_{3,8}^\ell}{\partial \mu^2} &= \bar{P}_{qq} \otimes T_{3,8}^\ell, \\
\mu^2 \frac{\partial V_{3,8}^\ell}{\partial \mu^2} &= \bar{P}_{qq} \otimes V_{3,8}^\ell,
\end{aligned} \tag{A.8}$$

where e_u and e_d are the electric charges of the up- and down-type quarks, n_f is the number of active quark flavours, n_u and n_d are the number of up- and down-type active quark flavours (such that $n_f = n_u + n_d$) and n_ℓ is the number of active leptons. Moreover, we have defined:

$$\begin{aligned}
e_\Sigma^2 &\equiv N_c(n_u e_u^2 + n_d e_d^2), \\
\delta_e^2 &\equiv N_c(n_u e_u^2 - n_d e_d^2), \\
\eta^\pm &\equiv \frac{1}{2} (e_u^2 \pm e_d^2),
\end{aligned} \tag{A.9}$$

being N_c the number of colours.

The basis presented here is implemented in **APFEL** and accessible through the **QUniD** solution.

References

- [1] **The NNPDF** Collaboration, R. D. Ball et al., *Parton distributions for the LHC Run II*, [arXiv:1410.8849](#).
- [2] L. Harland-Lang, A. Martin, P. Motylinski, and R. Thorne, *Parton distributions in the LHC era: MMHT 2014 PDFs*, [arXiv:1412.3989](#).
- [3] J. Gao, M. Guzzi, J. Huston, H.-L. Lai, Z. Li, et al., *CT10 next-to-next-to-leading order global analysis of QCD*, *Phys.Rev.* **D89** (2014), no. 3 033009, [[arXiv:1302.6246](#)].

- [4] **ZEUS, H1** Collaboration, H. Abramowicz et al., *Combination of Measurements of Inclusive Deep Inelastic $e^\pm p$ Scattering Cross Sections and QCD Analysis of HERA Data*, [arXiv:1506.06042](#).
- [5] S. Alekhin, J. Blumlein, and S. Moch, *The ABM parton distributions tuned to LHC data*, *Phys. Rev.* **D89** (2014), no. 5 054028, [[arXiv:1310.3059](#)].
- [6] A. Martin, R. Roberts, W. Stirling, and R. Thorne, *Parton distributions incorporating QED contributions*, *Eur.Phys.J.* **C39** (2005) 155–161, [[hep-ph/0411040](#)].
- [7] **NNPDF** Collaboration, R. D. Ball et al., *Parton distributions with QED corrections*, *Nucl.Phys.* **B877** (2013) 290–320, [[arXiv:1308.0598](#)].
- [8] S. Frixione, V. Hirschi, D. Pagani, H. S. Shao, and M. Zaro, *Weak corrections to Higgs hadroproduction in association with a top-quark pair*, *JHEP* **09** (2014) 065, [[arXiv:1407.0823](#)].
- [9] S. Frixione, V. Hirschi, D. Pagani, H. S. Shao, and M. Zaro, *Electroweak and QCD corrections to top-pair hadroproduction in association with heavy bosons*, *JHEP* **06** (2015) 184, [[arXiv:1504.03446](#)].
- [10] S. Kallweit, J. M. Lindert, P. Maierhöfer, S. Pozzorini, and M. Schönherr, *NLO electroweak automation and precise predictions for W +multijet production at the LHC*, *JHEP* **04** (2015) 012, [[arXiv:1412.5157](#)].
- [11] A. Denner, L. Hofer, A. Scharf, and S. Uccirati, *Electroweak corrections to lepton pair production in association with two hard jets at the LHC*, *JHEP* **01** (2015) 094, [[arXiv:1411.0916](#)].
- [12] M. Chiesa, N. Greiner, and F. Tramontano, *Electroweak corrections for LHC processes*, [arXiv:1507.08579](#).
- [13] V. Bertone, S. Carrazza, and J. Rojo, *APFEL: A PDF Evolution Library with QED corrections*, *Comput.Phys.Commun.* **185** (2014) 1647–1668, [[arXiv:1310.1394](#)].
- [14] A. Buckley, J. Ferrando, S. Lloyd, K. Nordström, B. Page, et al., *LHAPDF6: parton density access in the LHC precision era*, *Eur.Phys.J.* **C75** (2015), no. 3 132, [[arXiv:1412.7420](#)].
- [15] M. Roth and S. Weinzierl, *QED corrections to the evolution of parton distributions*, *Phys.Lett.* **B590** (2004) 190–198, [[hep-ph/0403200](#)].
- [16] **Particle Data Group** Collaboration, K. Olive et al., *Review of Particle Physics*, *Chin.Phys.* **C38** (2014) 090001.
- [17] S. Forte, E. Laenen, P. Nason, and J. Rojo, *Heavy quarks in deep-inelastic scattering*, *Nucl.Phys.* **B834** (2010) 116–162, [[arXiv:1001.2312](#)].
- [18] M. Aivazis, J. C. Collins, F. I. Olness, and W.-K. Tung, *Leptoproduction of heavy quarks. 2. A Unified QCD formulation of charged and neutral current processes from fixed target to collider energies*, *Phys.Rev.* **D50** (1994) 3102–3118, [[hep-ph/9312319](#)].
- [19] R. S. Thorne and R. G. Roberts, *An Ordered analysis of heavy flavor production in deep inelastic scattering*, *Phys. Rev.* **D57** (1998) 6871–6898, [[hep-ph/9709442](#)].
- [20] R. D. Ball, V. Bertone, S. Carrazza, C. S. Deans, L. Del Debbio, et al., *Parton distributions with LHC data*, *Nucl.Phys.* **B867** (2013) 244–289, [[arXiv:1207.1303](#)].
- [21] S. Carrazza, S. Forte, and J. Rojo, *Parton Distributions and Event Generators*, [arXiv:1311.5887](#).

- [22] J. Alwall, R. Frederix, S. Frixione, V. Hirschi, F. Maltoni, O. Mattelaer, H. S. Shao, T. Stelzer, P. Torrielli, and M. Zaro, *The automated computation of tree-level and next-to-leading order differential cross sections, and their matching to parton shower simulations*, *JHEP* **07** (2014) 079, [[arXiv:1405.0301](#)].
- [23] R. Boughezal, Y. Li, and F. Petriello, *Disentangling radiative corrections using the high-mass Drell-Yan process at the LHC*, *Phys. Rev.* **D89** (2014), no. 3 034030, [[arXiv:1312.3972](#)].
- [24] J. Baglio, L. D. Ninh, and M. M. Weber, *Massive gauge boson pair production at the LHC: a next-to-leading order story*, *Phys.Rev.* **D88** (2013) 113005, [[arXiv:1307.4331](#)].
- [25] W. Hollik, J. M. Lindert, E. Mirabella, and D. Pagani, *Electroweak corrections to squark-antisquark production at the LHC*, [arXiv:1506.01052](#).
- [26] **CMS** Collaboration, V. Khachatryan et al., *Reconstruction and identification of tau lepton decays to hadrons and tau neutrino at CMS*, [arXiv:1510.07488](#).
- [27] **ATLAS** Collaboration, G. Aad et al., *Search for high-mass diboson resonances with boson-tagged jets in proton-proton collisions at $\sqrt{s} = 8$ TeV with the ATLAS detector*, [arXiv:1506.00962](#).
- [28] A. Kulesza and W. J. Stirling, *Like sign W boson production at the LHC as a probe of double parton scattering*, *Phys.Lett.* **B475** (2000) 168–175, [[hep-ph/9912232](#)].
- [29] **CMS** Collaboration, S. Chatrchyan et al., *Missing transverse energy performance of the CMS detector*, *JINST* **6** (2011) P09001, [[arXiv:1106.5048](#)].
- [30] **CMS** Collaboration, V. Khachatryan et al., *Performance of the CMS missing transverse momentum reconstruction in pp data at $\sqrt{s} = 8$ TeV*, *JINST* **10** (2015), no. 02 P02006, [[arXiv:1411.0511](#)].
- [31] **ATLAS** Collaboration, G. Aad et al., *Performance of Missing Transverse Momentum Reconstruction in Proton-Proton Collisions at 7 TeV with ATLAS*, *Eur. Phys. J.* **C72** (2012) 1844, [[arXiv:1108.5602](#)].
- [32] *Expected performance of missing transverse momentum reconstruction for the ATLAS detector at $\sqrt{s} = 13$ TeV*, Tech. Rep. ATL-PHYS-PUB-2015-023, CERN, Geneva, Jul, 2015.
- [33] *Performance of missing transverse momentum reconstruction for the ATLAS detector in the first proton-proton collisions at $\sqrt{s} = 13$ TeV*, Tech. Rep. ATL-PHYS-PUB-2015-027, CERN, Geneva, Jul, 2015.
- [34] A. Djouadi, J.-L. Kneur, and G. Moultaka, *SuSpect: A Fortran code for the supersymmetric and Higgs particle spectrum in the MSSM*, *Comput. Phys. Commun.* **176** (2007) 426–455, [[hep-ph/0211331](#)].
- [35] G. Altarelli and G. Parisi, *Asymptotic Freedom in Parton Language*, *Nucl.Phys.* **B126** (1977) 298.
- [36] G. Curci, W. Furmanski, and R. Petronzio, *Evolution of Parton Densities Beyond Leading Order: The Nonsinglet Case*, *Nucl.Phys.* **B175** (1980) 27.
- [37] W. Furmanski and R. Petronzio, *Singlet Parton Densities Beyond Leading Order*, *Phys.Lett.* **B97** (1980) 437.
- [38] S. Moch, J. Vermaseren, and A. Vogt, *The Three loop splitting functions in QCD: The Nonsinglet case*, *Nucl.Phys.* **B688** (2004) 101–134, [[hep-ph/0403192](#)].

- [39] A. Vogt, S. Moch, and J. Vermaseren, *The Three-loop splitting functions in QCD: The Singlet case*, *Nucl.Phys.* **B691** (2004) 129–181, [[hep-ph/0404111](#)].